NADPH oxidase mediates microtubule alterations and diaphragm dysfunction in dystrophic mice

James A. Loehr[1], Shang Wang[1], Tanya R. Cully[1], Rituraj Pal[1], Irina V. Larina[1], Kirill V. Larin[1,2,3], and George G. Rodney[1*]

[1]Department of Molecular Physiology and Biophysics, Baylor College of Medicine, Houston, TX, 77030, [2]Department of Biomedical Engineering, University of Houston, Houston, TX, 77204, [3]Interdisciplinary Laboratory of Biophotonics, Tomsk State University, Tomsk 634050, Russia

[*]**Correspondence:**

Dr. George G. Rodney
Baylor College of Medicine
Department of Molecular Physiology & Biophysics
One Baylor Plaza-BCM335
Houston, TX, 77030, USA
713-798-5797
rodney@bcm.edu

Keywords: optical coherence elastography, microtubule, fibrosis, stiffness,

Abstract

Skeletal muscle from *mdx* mice is characterized by increased Nox2 ROS, altered microtubule network, increased muscle stiffness, and decreased muscle/respiratory function. While microtubule de-tyrosination has been suggested to increase stiffness and Nox2 ROS production in isolated single myofibers, its role in altering tissue stiffness and muscle function has not been established. Because Nox2 ROS production is upregulated prior to microtubule network alterations and ROS affect microtubule formation, we investigated the role of Nox2 ROS in diaphragm tissue microtubule organization, stiffness and muscle/respiratory function. Eliminating Nox2 ROS prevents microtubule disorganization and reduces fibrosis and muscle stiffness in *mdx* diaphragm. Fibrosis accounts for the majority of variance in diaphragm stiffness and decreased function, implicating altered extracellular matrix and not microtubule de-tyrosination as a modulator of diaphragm tissue function. Ultimately, inhibiting Nox2 ROS production increased force and respiratory function in dystrophic diaphragm, establishing Nox2 as a potential therapeutic target in Duchenne muscular dystrophy.

Introduction

Duchenne muscular dystrophy (DMD) is an X-linked recessive disease which affects 1 in every 3500 boys resulting in progressive muscle atrophy, loss of ambulation and cardio-respiratory failure (Levi, Genin, Angelini, Halevy, & Pines, 2015). In DMD patients, the leading cause of mortality is diaphragm dysfunction (Finder et al., 2004; Finsterer & Stöllberger, 2003; Percival et al., 2012). In the *mdx* animal, a mouse model of DMD, disease progression in the diaphragm mimics the human development of the disease (Stedman et al., 1991), and respiratory dysfunction has been shown to promote cardiac dysfunction (Barbin et al., 2016; Finder et al., 2004; Lanza et al., 2001).

NADPH Oxidase 2 (Nox2) has been shown to play an important role in dystrophic muscle. Nox2 content and activity are upregulated prior to the onset of inflammation and necrosis (N.P. Whitehead, Yeung, Froehner, & Allen, 2010) and downregulating Nox2 ROS production protects against pathophysiological alterations in young (5-7 wk) dystrophic muscle (Pal et al., 2014). Recent evidence indicates the microtubule (MT) network is dysregulated in dystrophic muscle (Belanto et al., 2016; Iyer et al., 2017; Khairallah et al., 2012; Prins et al., 2009), which results in aberrant Nox2 ROS production and implicates Nox2 ROS in altered mechanotransduction (Khairallah et al., 2012). However, Nox2 ROS is upregulated early (19 d; (N.P. Whitehead et al., 2010)), prior to changes in the MT network (Belanto et al., 2016; Iyer et al., 2017; Khairallah et al., 2012; Prins et al., 2009), and oxidation has been shown to be a post-translational modification of the MT network (Clark, Hagedorn, & Landino, 2014; Landino, Moynihan, Todd, & Kennett, 2004; Wilson & Gonzalez-Billault, 2015). These findings raise the question of whether Nox2 ROS initiates changes in the MT network.

In addition to increased Nox2 ROS production and alterations in the MT network, dystrophic muscle is characterized by increased fibrosis and muscle stiffness (Christophe Cornu, Goubel, & Fardeau, 1998; C. Cornu, Goubel, & Fardeau, 2001; Virgilio, Martin, Peirce, & Blemker, 2015). The de-tyrosination of α-tubulin (DT-tubulin) has been proposed as a mechanism which prevents the de-polymerization of the MT network, causing an increase in muscle stiffness and dysfunction in isolated muscle cells (Kerr et al., 2015; Robison et al., 2016). However, Belanto et al (Belanto et al., 2016) demonstrated increased muscle stiffness with no differences in relative DT-tubulin amount between *mdx* and WT mice. MT formation also is sensitive to the extracellular environment (Myers, Applegate, Danuser, Fischer, & Waterman, 2011; Andrew J. Putnam, Cunningham, Pillemer, & Mooney, 2003; A. J. Putnam, Schultz, & Mooney, 2001) and increased extracellular matrix (ECM) has been implicated in increased muscle stiffness and decreased force production (Desguerre et al., 2009; Meyer & Lieber, 2011; Percival et al., 2012; Rowe et al., 2010; Wood et al., 2014). Intriguingly, transgenic *mdx* mice expressing either a nearly full length dystrophin ($Dys^{\Delta 71\text{-}78}$-*mdx*) or overexpressing utrophin (*Fiona*) suggest that MT density and organization is independent of the level of MT de-tyrosination (Belanto et al., 2014; Belanto et al., 2016). Taken together, the role of de-tyrosinated MTs in tissue stiffness and disease pathogenesis in muscular dystrophy is unclear.

Skeletal muscle stiffness traditionally has been evaluated using either atomic force microscopy (AFM; (Canato et al., 2010; Kerr et al., 2015; Mathur, Collinsworth, Reichert, Kraus, & Truskey, 2001; van Zwieten et al., 2013)) or the passive properties of muscle measured during stretch (Chady H. Hakim & Duan, 2013; C. H. Hakim, Grange, & Duan, 2011; Lopez, Pardo, Cox, & Boriek, 2008; Rowe et al., 2010). AFM evaluates single muscle fiber stiffness but does not consider cell-cell interactions or the influence of the extra cellular matrix. While evaluating stiffness through muscle passive properties considers the series and parallel elastic components together it does not differentiate between the contributions of longitudinal (series) or transverse

(parallel) tissue stiffness within overall muscle stiffness. Optical coherence elastography (OCE) recently has been developed as a unique method to noninvasively evaluate tissue stiffness (Larin & Sampson, 2017; Wang & Larin, 2014; Wang et al., 2012; Wang et al., 2014). Here we utilize OCE to evaluate the differences in longitudinal and transverse tissue stiffness in the diaphragm of *mdx* mice. Previous data indicate *mdx* muscle is compromised in the transverse direction (Kumar, Khandelwal, Malya, Reid, & Boriek, 2004; Ramaswamy et al., 2011). Therefore, OCE may provide a unique method to differentiate pathological alterations in longitudinal and transverse stiffness and their impact on muscle function.

Because the altered MT network and fibrosis develop later in the disease pathology, after Nox2 ROS production has been initiated, we hypothesized that genetically eliminating Nox2 ROS production would prevent alterations to the MT network and reduce diaphragm stiffness thereby improving muscle and respiratory function in adult *mdx* mice. We also hypothesized, at the tissue level, stiffness would be greater in the transverse direction and fibrosis would be the major determinant of tissue stiffness.

Results

Genetic deletion of Nox2 ROS production prevents disorganization of the microtubule network in dystrophic muscle

Previous data have shown that tubulin content is upregulated in muscular dystrophy, and DT-tubulin may influence MT stability (Kerr et al., 2015; Khairallah et al., 2012; Prins et al., 2009). However, Belanto et al (Belanto et al., 2016) have suggested that the relative DT-tubulin level is not elevated in *mdx* muscle. Our data confirm that α-, β-, and DT-tubulin are elevated with muscular dystrophy and extend these findings to show that eliminating Nox2 ROS production in *mdx* mice prevents the increase in all three forms of tubulin (Fig. 1B-D). Because DT-tubulin is the de-tyrosinated form of α-tubulin, and both DT- and α-tubulin are elevated in *mdx* muscle, we assessed the fraction of α-tubulin that is de-tyrosinated. We found that there is no difference in the DT-/α-tubulin ratio between groups (Fig. 1E), suggesting that the increase in DT-tubulin is likely due to increased α-tubulin. Khairallah et al (Khairallah et al., 2012) demonstrated Nox2 ROS production is increased in response to a polymerized MT network. We found that Nox2 ROS production leads to increased MT disorganization (Fig 1G-H) and density (Fig 1I) in dystrophic diaphragm muscle which was prevented by eliminating Nox2 ROS. These results indicate that Nox2-generated ROS increases tubulin content, MT disorganization and MT polymerization in dystrophic diaphragm muscle and questions the role of DT-tubulin in MT stabilization or density.

Genetic inhibition of Nox2 ROS decreases skeletal muscle fibrosis

Increased fibrosis is a pathological hallmark of muscular dystrophy. In accordance with previous studies, we observed increased diaphragm fibrosis in *mdx* compared with WT mice (Fig 2). Eliminating Nox2 ROS in dystrophic muscle resulted in reduced collagen as measured by Trichrome staining (Fig 2A), hydroxyproline content (Fig 2B), and western blot (Fig 2C) as well as fibronectin content (Fig 2C). These data suggest that decreasing Nox2 ROS results in a significant decrease in fibrosis in the *mdx* diaphragm.

Muscle stiffness and stretch induced ROS are reduced in Nox2 deficient dystrophic muscle

Microtubules have been shown to be sensitive to the extracellular environment (Myers et al., 2011; Andrew J. Putnam et al., 2003; A. J. Putnam et al., 2001) and cell to cell (transverse) interactions are critical in skeletal muscle force transduction (Passerieux, Rossignol, Letellier, & Delage, 2007; Purslow & Trotter, 1994; Ramaswamy et al., 2011). We evaluated the role of Nox2 ROS in diaphragm mechanical properties using two distinct methods; passive stretch to

evaluate the series and parallel elastic components together and optical coherence elastography (OCE) to differentiate between the contributions of series (longitudinal stiffness) and parallel (transverse stiffness) components within overall muscle tissue stiffness. Figure 3A and E demonstrate the system design for both passive stretch and OCE, respectively, Figure 3F shows a sample OCT image of the diaphragm and Figure 3-video 1 illustrates a sample wave propagation taken during OCE. Passive stiffness while lengthening the diaphragm to 120% L_o was increased in *mdx* compared with WT mice, and eliminating Nox2 ROS resulted in reduced tissue stiffness compared with *mdx* diaphragm (Fig 3B-C). Transverse and longitudinal stiffness, using OCE, was increased in diaphragm of *mdx* mice compared with WT mice. Interestingly, eliminating Nox2 ROS production reduced only longitudinal stiffness in *Ncf1*$^{-/-}$::*mdx* (designated as p47$^{(-/-)}$/*mdx*) mice to WT levels (Fig. 3G-H). Muscle function was measured pre- and post-OCE to ensure OCE measurements did not compromise tissue health. Muscle function for all genotypes was not altered following OCE measurements (Fig. 3I). We also found that stretch induced ROS was elevated in *mdx* diaphragm compared with both WT and p47$^{(-/-)}$/*mdx* diaphragm tissue (Fig 3D). These data suggest that elevated Nox2 ROS increases diaphragm stiffness in dystrophic muscle and demonstrate Nox2 as the source of stretch induced ROS at the tissue level. In addition, stiffness measured using OCE can detect changes in tissue elastic properties based on fiber orientation and indicate a direction dependent response to alterations in tissue stiffness.

Fibrosis is a major determinant of diaphragm stiffness

Increased DT-tubulin has been suggested to stabilize the microtubule network resulting in less dynamic microtubules thereby increasing tissue stiffness (Kerr et al., 2015; Robison et al., 2016). Our results demonstrate that while both α- and DT-tubulin are upregulated in dystrophic muscle the ratio of DT- to α-tubulin revealed no significant difference between groups (Fig. 1E). A linear regression analysis demonstrated that fibrosis, DT-tubulin and α-tubulin significantly correlate to transverse and longitudinal diaphragm stiffness while the DT-/α-tubulin ratio only demonstrated a significant correlation with longitudinal stiffness (Table 1). A multiple linear regression analysis with either DT- or DT-/α-tubulin ratio and fibrosis revealed that the variance was no different than fibrosis alone (Table 1). Fibrosis accounted for 45% of the variance in the longitudinal and nearly 70% in the transverse direction. These data indicate while tubulin content correlates with muscle stiffness, fibrosis accounts for the majority of the variance in muscle stiffness at the tissue level.

Eliminating Nox2 ROS improves diaphragm muscle and respiratory function

Diaphragm muscle and respiratory function are compromised in *mdx* mice (Huang et al., 2011; Ishizaki et al., 2008; Pal et al., 2014; Percival et al., 2012). We previously have shown that eliminating Nox2 ROS production protected against diaphragm alterations in young (4-6 wks) *mdx* mice (Pal et al., 2014). Given muscle dysfunction in dystrophy is progressive, we wanted to determine whether eliminating Nox2 ROS provided protection against muscle/diaphragm dysfunction in older dystrophic mice. Here, we show that diaphragm function is impaired in adult (16-24 wks) *mdx* muscle and eliminating Nox2 ROS partially protected against the force deficits (Fig 4A). Eliminating Nox2 ROS in adult dystrophic muscle also protected against alterations in diaphragm fiber cross sectional area, fiber type and central nuclei (Figure 4- S2). These results, in combination with our previous data (Pal et al., 2014), indicate the lack of Nox2 ROS provides protection against pathophysiological alterations observed in dystrophic diaphragm muscle at different stages of disease pathology. In addition, eliminating Nox2 ROS protected against decrements in respiratory rate (f), minute ventilation (Mv), and peak inspiratory flow (PIF) in adult *mdx* mice (Table 3). A linear regression analysis demonstrated that fibrosis (Fig 4B) and both transverse and longitudinal diaphragm stiffness (Figure 4-figure supplement 2)

significantly correlated with peak diaphragm force. A multiple linear regression analysis revealed when either transverse or longitudinal diaphragm stiffness was included with fibrosis, the variance was no different than fibrosis alone (Table 2). These data indicate Nox2-derived ROS drive alterations in *mdx* diaphragm which lead to diaphragm and respiratory dysfunction.

Taxol induced MT polymerization has no effect on tissue stiffness but induced ROS production

To further elucidate the role of the MT network in tissue stiffness and ROS production, we incubated WT diaphragm with Taxol to polymerize the MT network. We observed similar alterations in the MT network between Taxol treated WT and *mdx* animals (Fig 1 F-I; Fig 5 A-D). Taxol increased MT density (Fig 5D) and resulted in disorganization of the MT network (Fig 5B-C). There was no difference in passive stiffness between Taxol and DMSO treated diaphragm tissue (Fig 5E-F); however, there was a difference in stretch induced ROS production (Fig 5G). These data, in combination with our previous data, support the idea that while alterations in the MT network increase ROS production, increases in DT-tubulin, MT density or MT disorganization do not influence tissue stiffness.

Discussion

Froehner and colleagues (Percival et al., 2007) originally demonstrated MT disorganization in dystrophic muscle and its subsequent restoration with the re-introduction of mini-dystrophin. In *mdx* mice, the MT network becomes altered at approximately 7-8 wks of age (Prins et al., 2009) and remains altered with age (9-11 months) (Kerr et al., 2015). It has been suggested that alterations in the MT network lead to increased Nox2 ROS production and altered mechanotransduction in adult *mdx* muscle (Kerr et al., 2015; Khairallah et al., 2012). However, Nox2 ROS is upregulated prior to changes in the MT network (Kerr et al., 2015; Prins et al., 2009; N.P. Whitehead et al., 2010), raising the question whether increased Nox2 ROS drives changes in the MT network. In neurons, tubulin oxidation prevents MT polymerization (Clark et al., 2014; Landino et al., 2004; Wilson & Gonzalez-Billault, 2015); however, it is unclear what role increased ROS production plays in modulating the MT network of skeletal muscle. Our data show that diaphragm MT alterations are increased in adult dystrophic muscle and eliminating Nox2 ROS prevented the increase in α-, β-, and DT-tubulin content (Fig. 1B-D), MT density (Fig. 1I), MT disorganization (Fig. 1G-H) and stiffness (Fig. 3C, G-H) observed in *mdx* mice. The MT network can be affected by muscle fiber type and regeneration (Percival et al., 2007; E. Ralston, Lu, & Ploug, 1999; Evelyn Ralston, Ploug, Kalhovde, & Lømo, 2001); both of which are altered in dystrophic muscle. Here we show that eliminating Nox2 ROS protected against alterations in fiber type switching and reduced central nuclei in dystrophic muscle. These data indicate Nox2 ROS, either directly or indirectly through alterations in fiber type or regeneration is modulating the MT network.

Previous work has focused on either the cortical (Percival et al.; Prins et al.) or some undetermined combination of the cortical and intermyofibrillar MT network (Kerr et al.; Khairallah et al.). However, given the intermyofibrillar MT network surrounds the contractile apparatus, any alterations to this network likely affect force production. In addition, Nox2 is located in the plasma membrane and 60-90% of the plasma membrane in skeletal muscle is comprised by the t-tubules (Eisenberg & Kuda; Mobley & Eisenberg; Peachey, 1965). Therefore, the intermyofibrillar MT network may contribute more to muscle function and the mechanical activation of Nox2 ROS compared with the cortical MT network. To further explore whether the altered intermyofibbrillar MT network influenced diaphragm stiffness and ROS

production we incubated WT diaphragm with Taxol. Polymerizing the MT network with Taxol resulted in increased intermyofibrillar MT density (Fig. 5D) and disorganization (Fig. 5B-C), similar to the diaphragm from *mdx* mice, but no change in tissue stiffness was detected. We found that Taxol increased stretch dependent ROS production at the tissue level (Fig. 5F); similar to what Khairallah et al has shown in single FDB fibers (Khairallah et al., 2012). Taken together, we show that Nox2 ROS is an early event that modulates the MT network, potentially resulting in a feed forward mechanism where elevated Nox2 ROS production increases MT density and disorganization which in turn leads to additional Nox2 ROS production. We currently are investigating the mechanisms by which Nox2 ROS modulates the MT network.

Respiratory insufficiency in the DMD patient is caused by respiratory muscle weakness, leading to impaired ventilation through an inability to inhale and exhale fully, ultimately resulting in a need for mechanical ventilation. Dystrophic muscle is characterized by increased fibrosis and while some show no link between altered collagen and stiffness (Chapman, Pichika, & Lieber, 2015; Smith & Barton, 2014) others have implicated fibrosis in decreased function and stiffness (Cabrera et al., 2014; Desguerre et al., 2009; Ishizaki et al., 2008; Mead et al., 2014; Meyer & Lieber, 2011; Percival et al., 2012; Rowe et al., 2010; Wood et al., 2014). Lateral force transmission through the endomysial layer of skeletal muscle has been shown to be important in overall force production (Passerieux et al., 2007; Patel & Lieber, 1997; Purslow & Trotter, 1994; Trotter & Purslow, 1992) and, in *mdx* mice, force is compromised in the transverse direction (Kumar et al., 2004; Ramaswamy et al., 2011). The endomysial layer also has increased levels of fibrosis which affects force production and correlates with the age of loss of ambulation in dystrophic muscle (Desguerre et al., 2012; Desguerre et al., 2009). Here we show decreased diaphragm muscle (Fig 4A) and respiratory function (Table 3) and increased fibrosis (Fig 2B) and tissue stiffness (Fig. 3 C, G-H) in dystrophic muscle. Eliminating Nox2 ROS in dystrophic diaphragm muscle reduced fibrosis and tissue stiffness, increased force and prevented the decline in respiratory function. Highlighting the importance of cell-cell interactions, our data demonstrate a stronger correlation between force and transverse stiffness (Fig S3) and fibrosis and transverse stiffness than longitudinal stiffness (Table 1). These data indicate that fibrosis is a crucial factor altering tissue stiffness and force production resulting in impaired cell-cell interactions. Furthermore, a 26% increase in diaphragm force maintained respiratory function in the p47$^{-/-}$/*mdx* mouse, likely decreasing the need to place patients on a ventilator.

Several therapeutics designed to reduce fibrosis have proved beneficial in improving muscle function in dystrophic muscle (Cabrera et al., 2014; Huebner, Jassal, Halevy, Pines, & Anderson, 2008; Percival et al., 2012; Turgeman et al., 2008; N. P. Whitehead, Kim, Bible, Adams, & Froehner, 2015). Therefore, based on our data, it is conceivable that decreased fibrosis reduces transverse muscle stiffness, improving lateral force transmission and thereby overall muscle function. In addition, it has been suggested that fibrosis induces a feed forward loop causing collagen producing myogenic cells not to differentiate into terminal satellite cells; inhibiting myogenesis and enhancing fibrosis (Alexakis, Partridge, & Bou-Gharios, 2007). These data are supported by the idea that progenitor cells take on a fibrogenic-like phenotype with aging; resulting in the loss of regenerative capacity in dystrophic muscle (Biressi, Miyabara, Gopinath, Carlig, & Rando, 2014; Pessina et al., 2015). The reduction in fibrosis observed by eliminating Nox2 ROS in dystrophic muscle may implicate a role for improved satellite cell activity given the reduced central nuclei (Fig S2C) and the increased CSA (Fig S2A) and Type 2B fibers (Fig S2E) observed in the p47$^{-/-}$/*mdx* mice. In addition, we previously demonstrated eliminating Nox2 ROS improves autophagy in dystrophic muscle (Pal et al., 2014) and autophagy is necessary for

satellite cell differentiation and fusion (Fortini et al., 2016). Future experiments are needed to investigate the role of Nox2 ROS in the impairment of satellite cell function

Tissue stiffness in leg muscle mirrors changes in the MT network; becoming altered in *mdx* animals at approximately 7-8 wks of age (Wolff et al., 2006) and remaining elevated in older animals (C. H. Hakim et al., 2011). Skeletal muscle stiffness has predominantly been assessed using atomic force microscopy (AFM) on single fibers (Canato et al., 2010; Kerr et al., 2015; Mathur et al., 2001; van Zwieten et al., 2013) or by passively lengthening muscle tissue (Chady H. Hakim & Duan, 2013; C. H. Hakim et al., 2011; Lopez et al., 2008; Rowe et al., 2010). In C2C12 cells and isolated adult myofibers, alterations to the MT network increased cell stiffness, measured via AFM, and altered mechanotransduction (Kerr et al., 2015; Khairallah et al., 2012). However, AFM uses a point specific bending moment evaluating only the near-membrane mechanical properties at that point (Kerr et al., 2015). While this approach is vital for understanding intracellular contributions to single cell signaling and near-membrane mechanics, it does not consider the ECM or cell-cell interactions in overall tissue mechanotransduction. Passive stretch takes into consideration both of these factors; however, it evaluates both the series (longitudinal) and parallel (transverse) elastic components together, making it difficult to assess the individual contributions to overall tissue stiffness. To address these limitations, we used two techniques to evaluate tissue stiffness, passive stretch and OCE. Interestingly, eliminating Nox2 ROS production partially prevented increases in tissue stiffness during passive lengthening (Fig 3C) similar to transverse stiffness measured using OCE (Fig 3G). In addition, we demonstrate a partial protection against force decrement (Fig 4A) and elevated transverse stiffness by eliminating Nox2 ROS production in the diaphragm (Fig 3G). These data highlight the importance of lateral (transverse) force transmission, and the significance of transverse stiffness in force production.

In isolated muscle cells, DT-tubulin, the de-tyrosinated form of α-tubulin, has been suggested to stabilize the MT network resulting in increased stiffness and reduced force (Kerr et al., 2015; Robison et al., 2016). However, MT formation is sensitive to alterations in the extracellular environment (Myers et al., 2011; Andrew J. Putnam et al., 2003; A. J. Putnam et al., 2001) implicating fibrosis in altering tissue stiffness. Previous work in neurons (Bartolini et al., 2016; Cook, Nagasaki, & Gundersen, 1998; Infante, Stein, Zhai, Borisy, & Gundersen, 2000; Khawaja, Gundersen, & Bulinski, 1988; Morris, Nader, Ramalingam, Bartolini, & Gundersen, 2014; Skoufias & Wilson, 1998; Webster, Wehland, Weber, & Borisy, 1990) indicates DT-tubulin simply occurs temporally at the same time but was not the cause of MT stabilization and in skeletal muscle, Belanto et al (Belanto et al., 2016) recently demonstrated while DT-tubulin was elevated in *mdx* quadriceps muscle, the fraction of DT-/α-tubulin was no different than WT mice. Our data support the idea that while DT-tubulin is elevated in dystrophic diaphragm the DT-/α-tubulin ratio is no different (Fig 1E), indicating elevated DT-tubulin is a function of elevated α-tubulin and not the cause of stabilized MTs. Using the DT-/α-tubulin ratio as the indicator of stabilized MTs, our data demonstrate a significant but weak correlation with OCE longitudinal diaphragm stiffness and no correlation with transverse stiffness (Table 1). When included with fibrosis, while elevated DT-tubulin and the DT-/α-tubulin ratio correlated with tissue stiffness, MLR revealed neither influenced diaphragm tissue stiffness above fibrosis. These data suggest neither the absolute nor the relative amount of DT-tubulin influence tissue stiffness and fibrosis is the main determinant of diaphragm tissue stiffness.

Nox2 protein level and ROS production are upregulated early in dystrophic muscle prior to the inflammatory response (Pal et al., 2014; N.P. Whitehead et al., 2010). Previously, we have shown that Nox2 ROS production initiates a feed forward loop exacerbating Nox2 ROS

production and inhibiting autophagic flux through activation of Src kinase (Pal et al., 2014). Interestingly, recent data by Froehner and colleagues (N. P. Whitehead, Kim, Bible, Adams, & Froehner, 2015) have shown that simvastatin reduced Nox2 protein levels, oxidative stress and fibrosis in *mdx* mice. Here we provide evidence for an additional feedforward mechanism where Nox2 ROS alters the MT network, which in turn exacerbates Nox2 ROS production. We also demonstrate that eliminating Nox2 ROS production alleviates many of the pathophysiological alterations, such as fibrosis, which occur in dystrophic diaphragm muscle. Taken together, there is compelling evidence that Nox2 ROS production is a central event in exacerbating disease pathology, implicating Nox2 as a viable therapeutic target in muscular dystrophy.

Materials and Methods

Animals

C57Bl/6J (WT) and C57Bl/10ScSn-Dmd*mdx*/J (*mdx*) were purchased from Jackson Laboratories (Bar Harbor, ME) and bred following their breeding strategy. Mice lacking $p47^{phox}$ (B6(Cg)-Ncf1m1J/J, JaxMice) were crossed with *mdx* mice to generate *Ncf1*$^{-/-}$::*mdx* (p47 $^{(-/-)}$/*mdx*) mice (Pal et al., 2014)). At approximately 5 months of age and in accordance with National Institutes of Health guidelines and approved by the Institutional Animal Care and Use Committee of Baylor College of Medicine, mice were anesthetized by isoflurane (2%) inhalation and euthanized by rapid cervical dislocation followed by thoracotomy.

Diaphragm passive stretch

Diaphragm muscle was surgically dissected and sectioned into diaphragm strips with the rib end attached to a fixed hook and the other to the lever arm of a dual-mode lever system (305C-LR-FP; Aurora Scientific Inc., Aurora, ON, Canada) using silk suture (4-0). The diaphragm was placed in a physiological saline solution containing (in mM): 2.0 CaCl2, 120.0 NaCl, 4.0 KCl, 1.0 MgSO4, 25.0 NaHCO3, 1.0 KH2PO4, 10.0 glucose, pH 7.3 and continuously gassed with 95% O2–5% CO2 at 25 °C. Muscle length was adjusted to elicit maximum twitch force (optimal length, L_o). A hand-held electronic caliper was used to measure L_o and the lever arm was programmed to passively stretch the diaphragm strip to 120% of L_o at 1 L_o/s for 5 min. At the end of the stretch protocol fiber bundles were removed from the rib, trimmed of excess connective tissue, blotted dry, and weighed. Muscle weight and L_o were used to estimate absolute forces expressed as N/cm^2 (Close, 1972).

To determine tissue stiffness, the Veronda-Westman model (Veronda & Westmann, 1970) was employed to quantify Young's modulus for the first stretch. The Veronda-Westman model describes a nonlinear relationship between stress and strain and previously has been utilized to study the elasticity of a number of biological tissues, such as breast and skin (Krouskop, Wheeler, Kallel, Garra, & Hall, 1998; Veronda & Westmann, 1970). Assuming the diaphragm tissue as an incompressible Veronda-Westman material, under uniaxial tension, the axial stress σ is related to the resulted stretch λ through equation 1: (Oberai et al., 2009; Pavan, Madsen, Frank, Adilton, & Hall, 2010)

$$\sigma = \frac{2E}{3}\left(\lambda^2 - \frac{1}{\lambda}\right)\left(e^{\gamma(\lambda^2+\frac{2}{\lambda}-3)} - \frac{1}{2\lambda}\right), \qquad \text{Eq. 1}$$

where $\lambda = 1+\varepsilon$ (ε is the strain), E is the Young's modulus of the diaphragm tissue at zero strain and γ is a nonlinear parameter representing the exponential increase rate of the Young's modulus over the increase of strain. Young's modulus was calculated through fitting the experimental data with Eq. 1 in Matlab (MathWorks; Natick, MA).

ROS Measurements

Diaphragm intracellular ROS was measured using 6-carboxy-2′,7′-dichlorodihydrofluorescein diacetate (DCFH-DA) (Invitrogen, Carlsbad, CA). Prior to stretch, the diaphragm was incubated with DCFH-DA for 30 min, washed using the physiological saline solution and de-esterified for an additional 30 min at 25°C. All cell-loading and imaging was performed in the dark to prevent light induced oxidation of DCFH-DA. A Sutter Lamda DG-5 Ultra high-speed wavelength switcher was used to excite DCF at 470/20 nm and emission intensity was collected at 535/48 nm on a charge coupled device (CCD) Camera (CoolSNAP MYO, Photometrics, Tucson, AZ) attached to an Axio Observer (Zeiss) inverted microscope (20× objective, 0.5 NA) at a rate of 0.2 Hz. Alterations in the rate of ROS production were baseline corrected and calculated over the final minute of the stretch period.

Effect of Taxol on Tissue Stiffness and ROS Production

WT diaphragm tissue was incubated with 20 μM Taxol (Sigma-Aldrich, St. Louis, MO) or DMSO (Sigma-Aldrich, St. Louis, MO) control for 2 hr at RT. After 1 hr the tissue was incubated with DCFH-DA, de-esterified and passively stretched as described above.

Optical coherence elastography

Optical coherence elastography (OCE) is a novel technique for nondestructive assessment of mechanical properties of tissues (Kennedy, Wijesinghe, & Sampson, 2017; Larin & Sampson, 2017). The principle of OCE is based on producing a pressure wave on the sample and monitoring the propagation of the wave using phase-sensitive optical coherence tomography (OCT) imaging on nanometer scale. The velocity of the wave propagation in different directions along the surface is used to deduct tissue elasticity anisotropically (Li, Guan, Huang, Johnstone, & Wang, 2012; Wang et al., 2012). A home-built OCE system was utilized which contains a focused air-puff device for tissue stimulation (Wang et al., 2013) and a spectral-domain OCT system to capture the tissue mechanical response (Wang et al., 2014). The air-puff system provided a highly-localized (~150 μm in diameter), short-duration (~1 ms), and low-pressure (below 10 Pa) air stream to stimulate the surface of the diaphragm tissue in a noncontact fashion. The induced tissue displacement had a micro-scale amplitude. The OCT system had an axial resolution of ~5 μm in tissue, an imaging beam diameter of ~4 μm at the focal plane, and a displacement sensitivity of ~11 nm with the phase of the OCT complex signal. The tissue displacement over time was detected using the temporal phase profile from the OCT system. A previously reported shear wave imaging OCT approach (Wang & Larin) was utilized to capture the elastic wave propagation in a depth-resolved 2D field of view with a time resolution of 16 μs. Cross-correlation of tissue displacement profiles was used to measure the time delay formed by the wave propagation at different locations. The elastic wave velocity was thus quantified based on the slope from a linear fit of the time delay with respect to the wave propagation distance. A surface wave model (Doyle, 1997) that relates the sample Young's modulus E to the wave velocity C was utilized to estimate the tissue elasticity through equation 2: (Li et al., 2012; Wang et al., 2012)

$$E = \frac{2\rho\times(1+\nu)^3\times C^2}{(0.87+1.12\nu)^2} \qquad \text{Eq. 2}$$

where ρ is the tissue density and ν is the Poisson's ratio; diaphragm density was 1060 kg/m^3 (Mendez & Keys, 1960). Due to the nearly incompressibility of soft tissue, the Poisson's ratio of 0.5 was utilized (Mathur et al., 2001). The averaged wave velocity value from 0-0.1 mm depth range from the tissue surface was used for calculation of the Young's modulus. For each

diaphragm sample, the elastic wave assessment was conducted in the transverse and longitudinal directions of the muscle fiber.

Ex vivo force measurements

Diaphragm muscle was surgically dissected from mice and sectioned into diaphragm strips with one end attached to a fixed hook and the other to a force transducer (F30, Harvard Apparatus) using silk suture (4-0) in a physiological saline solution continuously gassed with 95% O_2–5% CO_2 at 25°C. Diaphragm strips were incubated at 25°C for 10 min and optimal muscle length (L_o) and voltage (V_{max}) were adjusted to elicit maximum twitch force. Following a 5 min rest period, the diaphragm strip was stimulated at 150 Hz with pulse and train durations of 0.5 and 250 ms, respectively. Immediately after stimulation, L_o was determined using a hand-held electronic caliper and the diaphragm strip was placed at L_o in a 100 x 15 mm petri dish (VWR, Radnor, PA) for OCE measurements. Following OCE, the diaphragm was re-suspended from the force transducer at L_o and after a 5 min rest period stimulated again at 150 Hz to ensure OCE measurements did not compromise the diaphragms functional properties.

To determine the force-frequency relationship, diaphragm strips were incubated at 30°C for 15 min and L_o and V_{max} were adjusted to elicit maximum twitch force. Following a 5 min rest period, force-frequency characteristics were measured at stimulation frequencies of 1, 5, 10, 20, 40, 60, 80, and 100-Hz every minute with pulse and train durations of 0.5 and 250 ms. At the end of the contractile protocol L_o was measured using a hand-held electronic caliper. Following both stimulation protocols, fiber bundles were trimmed of excess bone and connective tissue, blotted dry, and weighed. Muscle weight and L_o were used to estimate cross-sectional area and absolute forces expressed as N/cm^2 (Close).

Unrestrained whole-body plethysmography

Respiratory function was monitored in unrestrained mice using Buxco small animal whole-body plethysmography (Data Sciences International, New Brighton, MN) and FinePointe software (Data Sciences International, New Brighton, MN). The system was calibrated each day prior to data collection. On the day of data collection, animals were placed in individual chambers and given 30 min to acclimate; followed by 60 min of data collection. The software averaged the data over each minute and recorded a value every minute for 60 min. To ensure data was representative, breath frequency was used to ensure the mouse had not held its breath, buried its head under its body or was breathing too rapidly. Mean breath frequency was calculated and data which fell outside 1SD of the mean was excluded from the data analysis (Roberts, Holley-Cuthrell, Gonzalez-Vega, Mull, & Heydemann, 2015).

Western Blot

Lysates from diaphragm tissue were extracted and quantified with the bicinchoninic acid (BCA) protein assay kit (Pierce, Rockford, IL), using BSA as the standard. Lysates were separated via SDS-PAGE and transferred to polyvinyldifluoride (PVDF) membranes. All tubulin blots were incubated in blocking buffer (5%, w/v, dried skimmed milk in Tris-buffered saline, pH 7.4, and 0.2% Tween 20; TBST) for 60 min and incubated overnight with anti-α-tubulin (Santa Cruz Biotechnologies), anti-β-tubulin (Cell Signaling Technology), anti-detyrosinatedtubulin (Millipore) and anti-GAPDH (Millipore) in blocking buffer. Fibronectin and collagen blots were blocked for 60 min in blocking buffer as above except with .05% Tween 20 and incubated with anti-fibronectin (Millipore), anti-collagen (Abcam) and anti-GAPDH for 60 min at room temperature (RT). Tubulin and fibronectin blots were exposed to IRDye® Secondary Antibodies (LI-COR Biosciences) diluted in TBST for 60 min at RT and washed again. The LI-COr® Odyssey Infrared Imaging System was used for blot detection and ImageJ software for blot

analysis. The collagen blot was probed with secondary antibodies; ECL anti-mouse IgG HRP (NA931, GE Healthcare) and ECL Anti-rabbit IgG HRP (NA93401, GE Healthcare) for 60 min at RT. The membrane was imaged using the Chemidoc touch with Clarity and Clarity Max ECL reagent (Bio-Rad, Hercules, CA). Image analysis was performed using Biorad Image Lab 6.0 software.

Hydroxyproline Assay

Diaphragm collagen content was measured using a hydroxyproline assay kit (Sigma-Aldrich, St. Louis, MO). Briefly, diaphragm tissue was homogenized and hydrolyzed in 200 µl of 6 M hydrochloric acid at 100 °C for 3 hours. Hydrolysate was transferred to a 96-well plate (Corning, Corning, NY) and evaporated in an oven at 60 °C. Following evaporation, the Chloromine T/Oxidation Buffer mixture was added to all wells and incubated for 5 min at RT. DMAB (4-(Dimethylamino) benzaldehyde) was diluted in a Perchloric Acid/Isopropanol solution, added to all wells, and incubated for 90 min at 60 °C. A hydroxyproline standard curve (0-1.0 µg) was included in the assay to quantify hydroxyproline content in each sample. All samples, including the standard curve, were performed in duplicate and absorbance was measured at 560 nm. Results are reported as µg of hydroxyproline per mg of tissue (µg/mg).

Immunofluorescence

For fiber-type, serial diaphragm sections of 12-14 µm thickness were sectioned at −24°C using a refrigerated cryostat (Shandon Cryotome E, Thermo). Sections were fixed with cold methanol for 20 min and incubated overnight in a humid box at 4°C with Anti-Type I (BA-F8) and anti-Type IIA (SC-71) antibodies purchased from Developmental Studies Hybridoma Bank (DSHB; Iowa City, IA). Sections were then incubated for 3 hours with IgG1 and IgG2b isotype-specific secondary antibodies (Invitrogen, Waltham, MA). Slides were mounted with VECTASHIELD anti-fade mounting media containing DAPI (Vector Laboratories, Berlingame, CA). Images were acquired using a CCD camera (Digital Sight DS-Fi1, Nikon) attached to an upright microscope (Nikon Eclipse 80i, 10× objective, 0.45 NA). Images were analyzed using ImageJ software.

For α–tubulin staining, diaphragm tissue was fixed at L_o using 10% neutral buffered formalin (VWR, Radnor, PA) for 2h at room temperature. The tissue was rinsed 3 times and stored in PBS (ThermoScientific, Waltham, MA) plus 1 mM EDTA (Invitrogen, Waltham, MA). Diaphragm fibers were mechanically dissociated from the fixed diaphragm strip into single fibers and placed in 35 mm glass bottom culture dishes (MatTek, Ashland, MA) containing PBS plus 1 mM EDTA. Fibers were permeabilized with 0.1% Triton X-100 in PBS plus 1 mM EDTA for 10 min. After rinsing three times with PBS plus 1 mM EDTA, a blocking agent was added (0.1% saponin, 10% FBS in PBS plus 1 mM EDTA) for 1 h at RT. Fibers were incubated with an Alexa-Fluor 488 conjugated α-tubulin antibody (Life Technologies, Waltham, MA) for 2 d at 4 °C. Diaphragm fibers were washed with PBS and mounted with VECTASHIELD anti- fade mounting media containing DAPI (Vector Laboratories, Berlingame, CA) prior to microscopy. Fibers were imaged using a Zeiss LSM 780 confocal microscope (Zeiss, Oberkochen, Germany). Microtubule organization was analyzed using custom software (Liu & Ralston, 2014) and microtubule density was assessed by summing 10 images from the intra-myofibrillar region of each fiber (> 3 µm from surface), converted to a binary image and quantified using ImageJ software. Images were subjected to background subtraction and contrast enhancement using Image J for figure presentation only.

Histology

Using a refrigerated cryostat (Shandon Cryotome E, Thermo), 12-14 µm thick serial sections were cut from the mid-belly region of the diaphragm at −24°C. Sections were stained using

Masson's Trichrome for fibrosis and Hematoxylin and Eosin for cross sectional area (CSA) and centralized nuclei. Images were acquired using a CCD camera (Digital Sight DS-Fi1, Nikon) attached to an upright microscope (Nikon Eclipse 80i, 10× objective, 0.45 NA). Images were analyzed using ImageJ software.

Statistical Analysis

Data are reported as mean ± SEM, unless otherwise specified. A 1-way ANOVA was used to measure statistical differences between groups. A 2-way RM ANOVA was used to determine statistical differences between groups for the force-frequency data. For CSA, a Kruskal-Wallis ANOVA was used to determine differences between groups. Tukey's post-hoc test was used when statistical differences were identified. Linear regression and multiple linear regression models were used to determine correlations between variables. Statistical analysis was performed in Origin Pro (OriginLab Corporation, Northhampton, MA) with significance set *a priori* at $p \leq 0.05$.

Acknowledgement

The authors would like to thank Drs. Wenhua Liu and Evelyn Ralston (National Institute of Arthritis and Musculoskeletal and Skin Diseases) for providing the directionality analysis program. Research reported in this publication was supported by the National Institute of Arthritis and Musculoskeletal and Skin Diseases of the National Institutes of Health under Award Number R01 AR061370 to G.G.R, the National Heart, Lung, and Blood Institute of the National Institutes of Health under Award Number R01 HL120140 to K.V.L. and I.V.L. and T32 HL007676 to J.A.L. Additional support was provided by the National Eye Institute of the National Institutes of Health under Award Number R01 EY022362 to K.V.L., the American Heart Association under Award Number 16POST30990070 to S.W., and a Gillson Longenbaugh Foundation Award to G.G.R.

Competing Interests

The authors have no financial or non-financial competing interests to disclose.

References

Alexakis, C., Partridge, T., & Bou-Gharios, G. (2007). Implication of the satellite cell in dystrophic muscle fibrosis: a self-perpetuating mechanism of collagen overproduction. *Am J Physiol Cell Physiol, 293*(2), C661-669. doi:10.1152/ajpcell.00061.2007

Barbin, I. C., Pereira, J. A., Bersan Rovere, M., de Oliveira Moreira, D., Marques, M. J., & Santo Neto, H. (2016). Diaphragm degeneration and cardiac structure in mdx mouse: potential clinical implications for Duchenne muscular dystrophy. *J Anat, 228*(5), 784-791. doi:10.1111/joa.12443

Bartolini, F., Andres-Delgado, L., Qu, X., Nik, S., Ramalingam, N., Kremer, L., . . . Gundersen, G. G. (2016). An mDia1-INF2 formin activation cascade facilitated by IQGAP1 regulates stable microtubules in migrating cells. *Mol Biol Cell, 27*(11), 1797-1808. doi:10.1091/mbc.E15-07-0489

Belanto, J. J., Mader, T. L., Eckhoff, M. D., Strandjord, D. M., Banks, G. B., Gardner, M. K., . . . Ervasti, J. M. (2014). Microtubule binding distinguishes dystrophin from utrophin. *Proc Natl Acad Sci U S A, 111*(15), 5723-5728. doi:10.1073/pnas.1323842111

Belanto, J. J., Olthoff, J. T., Mader, T. L., Chamberlain, C. M., Nelson, D. M., McCourt, P. M., . . . Ervasti, J. M. (2016). Independent variability of microtubule perturbations associated with dystrophinopathy. *Hum Mol Genet, 25*(22), 4951-4961. doi:10.1093/hmg/ddw318

Biressi, S., Miyabara, E. H., Gopinath, S. D., Carlig, P. M., & Rando, T. A. (2014). A Wnt-TGFbeta2 axis induces a fibrogenic program in muscle stem cells from dystrophic mice. *Sci Transl Med, 6*(267), 267ra176. doi:10.1126/scitranslmed.3008411

643 Cabrera, D., Gutiérrez, J., Cabello-Verrugio, C., Morales, M. G., Mezzano, S., Fadic, R., . . . Brandan, E.
644 (2014). Andrographolide attenuates skeletal muscle dystrophy in mdx mice and increases
645 efficiency of cell therapy by reducing fibrosis. *Skeletal Muscle, 4*, 6-6. doi:10.1186/2044-5040-4-
646 6
647 Canato, M., Dal Maschio, M., Sbrana, F., Raiteri, R., Reggiani, C., Vassanelli, S., & Megighian, A. (2010).
648 Mechanical and Electrophysiological Properties of the Sarcolemma of Muscle Fibers in Two
649 Murine Models of Muscle Dystrophy: Col6a1−/− and Mdx. *Journal of Biomedicine and*
650 *Biotechnology, 2010*, 981945. doi:10.1155/2010/981945
651 Chapman, M. A., Pichika, R., & Lieber, R. L. (2015). Collagen crosslinking does not dictate stiffness in a
652 transgenic mouse model of skeletal muscle fibrosis. *J Biomech, 48*(2), 375-378.
653 doi:10.1016/j.jbiomech.2014.12.005
654 Clark, H. M., Hagedorn, T. D., & Landino, L. M. (2014). Hypothiocyanous acid oxidation of tubulin
655 cysteines inhibits microtubule polymerization. *Archives of biochemistry and biophysics, 541*,
656 10.1016/j.abb.2013.1010.1026. doi:10.1016/j.abb.2013.10.026
657 Close, R. I. (1972). Dynamic properties of mammalian skeletal muscles. *Physiol Rev., 52*(1), 129-197.
658 Cook, T. A., Nagasaki, T., & Gundersen, G. G. (1998). Rho guanosine triphosphatase mediates the
659 selective stabilization of microtubules induced by lysophosphatidic acid. *J Cell Biol, 141*(1), 175-
660 185.
661 Cornu, C., Goubel, F., & Fardeau, M. (1998). Stiffness of knee extensors in Duchenne Muscular
662 Dystrophy. *Muscle & Nerve, 21*(12), 1772-1774. doi:10.1002/(SICI)1097-
663 4598(199812)21:12<1772::AID-MUS21>3.0.CO;2-0
664 Cornu, C., Goubel, F., & Fardeau, M. (2001). Muscle and joint elastic properties during elbow flexion in
665 Duchenne muscular dystrophy. *J Physiol, 533*(Pt 2), 605-616.
666 Desguerre, I., Arnold, L., Vignaud, A., Cuvellier, S., Yacoub-Youssef, H., Gherardi, R. K., . . . Chazaud, B.
667 (2012). A new model of experimental fibrosis in hindlimb skeletal muscle of adult mdx mouse
668 mimicking muscular dystrophy. *Muscle Nerve, 45*(6), 803-814. doi:10.1002/mus.23341
669 Desguerre, I., Mayer, M., Leturcq, F., Barbet, J. P., Gherardi, R. K., & Christov, C. (2009). Endomysial
670 fibrosis in Duchenne muscular dystrophy: a marker of poor outcome associated with
671 macrophage alternative activation. *J Neuropathol Exp Neurol, 68*(7), 762-773.
672 doi:10.1097/NEN.0b013e3181aa31c2
673 Doyle, J. F. (1997). *Wave propagation in structure: spectral analysis using fast discrete Fourier*
674 *transforms*.
675 Eisenberg, B. R., & Kuda, A. M. (1975). Stereological analysis of mammalian skeletal muscle. II. White
676 vastus muscle of the adult guinea pig. *J Ultrastruct Res, 51*(2), 176-187.
677 Finder, J. D., Birnkrant, D., Carl, J., Farber, H. J., Gozal, D., Iannaccone, S. T., . . . American Thoracic, S.
678 (2004). Respiratory care of the patient with Duchenne muscular dystrophy: ATS consensus
679 statement. *Am J Respir Crit Care Med, 170*(4), 456-465. doi:10.1164/rccm.200307-885ST
680 Finsterer, J., & Stöllberger, C. (2003). The Heart in Human Dystrophinopathies. *Cardiology, 99*(1), 1-19.
681 doi:10.1159/000068446
682 Fortini, P., Ferretti, C., Iorio, E., Cagnin, M., Garribba, L., Pietraforte, D., . . . Dogliotti, E. (2016). The fine
683 tuning of metabolism, autophagy and differentiation during in vitro myogenesis. *Cell Death Dis,*
684 *7*, e2168. doi:10.1038/cddis.2016.50
685 Hakim, C. H., & Duan, D. (2013). Truncated dystrophins reduce muscle stiffness in the extensor
686 digitorum longus muscle of mdx mice. *Journal of Applied Physiology, 114*(4), 482-489.
687 doi:10.1152/japplphysiol.00866.2012
688 Hakim, C. H., Grange, R. W., & Duan, D. (2011). The passive mechanical properties of the extensor
689 digitorum longus muscle are compromised in 2- to 20-mo-old mdx mice. *J Appl Physiol (1985),*
690 *110*(6), 1656-1663. doi:10.1152/japplphysiol.01425.2010
691 Huang, P., Cheng, G., Lu, H., Aronica, M., Ransohoff, R. M., & Zhou, L. (2011). Impaired respiratory
692 function in mdx and mdx/utrn(+/-) mice. *Muscle Nerve, 43*(2), 263-267. doi:10.1002/mus.21848

693 Huebner, K. D., Jassal, D. S., Halevy, O., Pines, M., & Anderson, J. E. (2008). Functional resolution of
694 fibrosis in mdx mouse dystrophic heart and skeletal muscle by halofuginone. *Am J Physiol Heart*
695 *Circ Physiol, 294*(4), H1550-1561. doi:10.1152/ajpheart.01253.2007
696 Infante, A. S., Stein, M. S., Zhai, Y., Borisy, G. G., & Gundersen, G. G. (2000). Detyrosinated (Glu)
697 microtubules are stabilized by an ATP-sensitive plus-end cap. *J Cell Sci, 113 (Pt 22)*, 3907-3919.
698 Ishizaki, M., Suga, T., Kimura, E., Shiota, T., Kawano, R., Uchida, Y., . . . Uchino, M. (2008). Mdx
699 respiratory impairment following fibrosis of the diaphragm. *Neuromuscul Disord, 18*(4), 342-348.
700 doi:10.1016/j.nmd.2008.02.002
701 Iyer, S. R., Shah, S. B., Valencia, A. P., Schneider, M. F., Hernandez-Ochoa, E. O., Stains, J. P., . . . Lovering,
702 R. M. (2017). Altered nuclear dynamics in MDX myofibers. *J Appl Physiol (1985), 122*(3), 470-481.
703 doi:10.1152/japplphysiol.00857.2016
704 Kennedy, B. F., Wijesinghe, P., & Sampson, D. D. (2017). The emergence of optical elastography in
705 biomedicine. *Nature Photonics, 11*, 215. doi:10.1038/nphoton.2017.6
706 Kerr, J. P., Robison, P., Shi, G., Bogush, A. I., Kempema, A. M., Hexum, J. K., . . . Ward, C. W. (2015).
707 Detyrosinated microtubules modulate mechanotransduction in heart and skeletal muscle. *Nat*
708 *Commun, 6*, 8526. doi:10.1038/ncomms9526
709 Khairallah, R. J., Shi, G., Sbrana, F., Prosser, B. L., Borroto, C., Mazaitis, M. J., . . . Ward, C. W. (2012).
710 Microtubules underlie dysfunction in duchenne muscular dystrophy. *Sci.Signal., 5*(236), ra56.
711 doi:5/236/ra56 [pii];10.1126/scisignal.2002829 [doi]
712 Khawaja, S., Gundersen, G. G., & Bulinski, J. C. (1988). Enhanced stability of microtubules enriched in
713 detyrosinated tubulin is not a direct function of detyrosination level. *J Cell Biol, 106*(1), 141-149.
714 Krouskop, T. A., Wheeler, T. M., Kallel, F., Garra, B. S., & Hall, T. (1998). Elastic moduli of breast and
715 prostate tissues under compression. *Ultrason Imaging, 20*(4), 260-274.
716 doi:10.1177/016173469802000403
717 Kumar, A., Khandelwal, N., Malya, R., Reid, M. B., & Boriek, A. M. (2004). Loss of dystrophin causes
718 aberrant mechanotransduction in skeletal muscle fibers. *FASEB J, 18*(1), 102-113.
719 doi:10.1096/fj.03-0453com
720 Landino, L. M., Moynihan, K. L., Todd, J. V., & Kennett, K. L. (2004). Modulation of the redox state of
721 tubulin by the glutathione/glutaredoxin reductase system. *Biochemical and Biophysical Research*
722 *Communications, 314*(2), 555-560. doi:http://dx.doi.org/10.1016/j.bbrc.2003.12.126
723 Lanza, G. A., Russo, A. D., Giglio, V., De Luca, L., Messano, L., Santini, C., . . . Bellocci, F. (2001).
724 Impairment of cardiac autonomic function in patients with Duchenne muscular dystrophy:
725 Relationship to myocardial and respiratory function. *American Heart Journal, 141*(5), 808-812.
726 doi:http://dx.doi.org/10.1067/mhj.2001.114804
727 Larin, K. V., & Sampson, D. D. (2017). Optical coherence elastography - OCT at work in tissue
728 biomechanics [Invited]. *Biomed Opt Express, 8*(2), 1172-1202. doi:10.1364/BOE.8.001172
729 Levi, O., Genin, O., Angelini, C., Halevy, O., & Pines, M. (2015). Inhibition of muscle fibrosis results in
730 increases in both utrophin levels and the number of revertant myofibers in Duchenne muscular
731 dystrophy. *Oncotarget, 6*(27), 23249-23260.
732 Li, C., Guan, G., Huang, Z., Johnstone, M., & Wang, R. K. (2012). Noncontact all-optical measurement of
733 corneal elasticity. *Opt Lett, 37*(10), 1625-1627. doi:10.1364/OL.37.001625
734 Liu, W., & Ralston, E. (2014). A new directionality tool for assessing microtubule pattern alterations.
735 *Cytoskeleton (Hoboken), 71*(4), 230-240. doi:10.1002/cm.21166
736 Lopez, M. A., Pardo, P. S., Cox, G. A., & Boriek, A. M. (2008). Early mechanical dysfunction of the
737 diaphragm in the muscular dystrophy with myositis (Ttnmdm) model. *Am J Physiol Cell Physiol,*
738 *295*(5), C1092-1102. doi:10.1152/ajpcell.16.2008
739 Mathur, A. B., Collinsworth, A. M., Reichert, W. M., Kraus, W. E., & Truskey, G. A. (2001). Endothelial,
740 cardiac muscle and skeletal muscle exhibit different viscous and elastic properties as determined
741 by atomic force microscopy. *J Biomech, 34*(12), 1545-1553.
742 Mead, A. F., Petrov, M., Malik, A. S., Mitchell, M. A., Childers, M. K., Bogan, J. R., . . . Stedman, H. H.
743 (2014). Diaphragm remodeling and compensatory respiratory mechanics in a canine model of

744 Duchenne muscular dystrophy. *Journal of Applied Physiology, 116*(7), 807-815.
745 doi:10.1152/japplphysiol.00833.2013
746 Mendez, J., & Keys, A. (1960). Density and composition of mammalian muscle. *Metabolism, 9*, 184-188.
747 Meyer, G. A., & Lieber, R. L. (2011). Elucidation of extracellular matrix mechanics from muscle fibers and
748 fiber bundles. *J Biomech, 44*(4), 771-773. doi:10.1016/j.jbiomech.2010.10.044
749 Mobley, B. A., & Eisenberg, B. R. (1975). Sizes of components in frog skeletal muscle measured by
750 methods of stereology. *J Gen Physiol, 66*(1), 31-45.
751 Morris, E. J., Nader, G. P., Ramalingam, N., Bartolini, F., & Gundersen, G. G. (2014). Kif4 interacts with
752 EB1 and stabilizes microtubules downstream of Rho-mDia in migrating fibroblasts. *PLoS ONE,*
753 *9*(3), e91568. doi:10.1371/journal.pone.0091568
754 Myers, K. A., Applegate, K. T., Danuser, G., Fischer, R. S., & Waterman, C. M. (2011). Distinct ECM
755 mechanosensing pathways regulate microtubule dynamics to control endothelial cell branching
756 morphogenesis. *The Journal of Cell Biology, 192*(2), 321-334. doi:10.1083/jcb.201006009
757 Oberai, A. A., Gokhale, N. H., Goenezen, S., Barbone, P. E., Hall, T. J., Sommer, A. M., & Jiang, J. (2009).
758 Linear and nonlinear elasticity imaging of soft tissue in vivo: demonstration of feasibility. *Phys*
759 *Med Biol, 54*(5), 1191-1207. doi:10.1088/0031-9155/54/5/006
760 Pal, R., Palmieri, M., Loehr, J. A., Li, S., Abo-Zahrah, R., Monroe, T. O., . . . Rodney, G. G. (2014). Src-
761 dependent impairment of autophagy by oxidative stress in a mouse model of Duchenne
762 muscular dystrophy. *Nat Commun, 5*, 4425. doi:10.1038/ncomms5425
763 Passerieux, E., Rossignol, R., Letellier, T., & Delage, J. P. (2007). Physical continuity of the perimysium
764 from myofibers to tendons: involvement in lateral force transmission in skeletal muscle. *J Struct*
765 *Biol, 159*(1), 19-28. doi:10.1016/j.jsb.2007.01.022
766 Patel, T. J., & Lieber, R. L. (1997). Force transmission in skeletal muscle: from actomyosin to external
767 tendons. *Exerc Sport Sci Rev, 25*, 321-363.
768 Pavan, T. Z., Madsen, E. L., Frank, G. R., Adilton, O. C. A., & Hall, T. J. (2010). Nonlinear elastic behavior of
769 phantom materials for elastography. *Phys Med Biol, 55*(9), 2679-2692. doi:10.1088/0031-
770 9155/55/9/017
771 Peachey, L. D. (1965). The sarcoplasmic reticulum and transverse tubules of the frog's sartorius. *J Cell*
772 *Biol, 25*(3), Suppl:209-231.
773 Percival, J. M., Gregorevic, P., Odom, G. L., Banks, G. B., Chamberlain, J. S., & Froehner, S. C. (2007).
774 rAAV6-microdystrophin rescues aberrant Golgi complex organization in mdx skeletal muscles.
775 *Traffic, 8*(10), 1424-1439. doi:10.1111/j.1600-0854.2007.00622.x
776 Percival, J. M., Whitehead, N. P., Adams, M. E., Adamo, C. M., Beavo, J. A., & Froehner, S. C. (2012).
777 Sildenafil reduces respiratory muscle weakness and fibrosis in the mdx mouse model of
778 Duchenne muscular dystrophy. *J Pathol, 228*(1), 77-87. doi:10.1002/path.4054
779 Pessina, P., Kharraz, Y., Jardi, M., Fukada, S., Serrano, A. L., Perdiguero, E., & Munoz-Canoves, P. (2015).
780 Fibrogenic Cell Plasticity Blunts Tissue Regeneration and Aggravates Muscular Dystrophy. *Stem*
781 *Cell Reports, 4*(6), 1046-1060. doi:10.1016/j.stemcr.2015.04.007
782 Prins, K. W., Humston, J. L., Mehta, A., Tate, V., Ralston, E., & Ervasti, J. M. (2009). Dystrophin is a
783 microtubule-associated protein. *The Journal of Cell Biology, 186*(3), 363-369.
784 doi:10.1083/jcb.200905048
785 Purslow, P. P., & Trotter, J. A. (1994). The morphology and mechanical properties of endomysium in
786 series-fibred muscles: variations with muscle length. *J Muscle Res Cell Motil, 15*(3), 299-308.
787 Putnam, A. J., Cunningham, J. J., Pillemer, B. B. L., & Mooney, D. J. (2003). *External mechanical strain*
788 *regulates membrane targeting of Rho GTPases by controlling microtubule assembly* (Vol. 284).
789 Putnam, A. J., Schultz, K., & Mooney, D. J. (2001). Control of microtubule assembly by extracellular
790 matrix and externally applied strain. *Am J Physiol Cell Physiol, 280*(3), C556-564.
791 Ralston, E., Lu, Z., & Ploug, T. (1999). The organization of the Golgi complex and microtubules in skeletal
792 muscle is fiber type-dependent. *J Neurosci, 19*(24), 10694-10705.

Ralston, E., Ploug, T., Kalhovde, J., & Lømo, T. (2001). Golgi Complex, Endoplasmic Reticulum Exit Sites, and Microtubules in Skeletal Muscle Fibers Are Organized by Patterned Activity. *The Journal of Neuroscience, 21*(3), 875-883.

Ramaswamy, K. S., Palmer, M. L., van der Meulen, J. H., Renoux, A., Kostrominova, T. Y., Michele, D. E., & Faulkner, J. A. (2011). Lateral transmission of force is impaired in skeletal muscles of dystrophic mice and very old rats. *The Journal of Physiology, 589*(Pt 5), 1195-1208. doi:10.1113/jphysiol.2010.201921

Roberts, N. W., Holley-Cuthrell, J., Gonzalez-Vega, M., Mull, A. J., & Heydemann, A. (2015). Biochemical and Functional Comparisons of mdx and Sgcg(-/-) Muscular Dystrophy Mouse Models. *Biomed Res Int, 2015*, 131436. doi:10.1155/2015/131436

Robison, P., Caporizzo, M. A., Ahmadzadeh, H., Bogush, A. I., Chen, C. Y., Margulies, K. B., . . . Prosser, B. L. (2016). Detyrosinated microtubules buckle and bear load in contracting cardiomyocytes. *Science, 352*(6284), aaf0659. doi:10.1126/science.aaf0659

Rowe, J., Chen, Q., Domire, Z. J., McCullough, M. B., Sieck, G., Zhan, W. Z., & An, K. N. (2010). Effect of collagen digestion on the passive elastic properties of diaphragm muscle in rat. *Med Eng Phys, 32*(1), 90-94. doi:10.1016/j.medengphy.2009.11.002

Skoufias, D. A., & Wilson, L. (1998). Assembly and colchicine binding characteristics of tubulin with maximally tyrosinated and detyrosinated alpha-tubulins. *Arch Biochem Biophys, 351*(1), 115-122. doi:10.1006/abbi.1997.0510

Smith, L. R., & Barton, E. R. (2014). Collagen content does not alter the passive mechanical properties of fibrotic skeletal muscle in mdx mice. *Am J Physiol Cell Physiol, 306*(10), C889-898. doi:10.1152/ajpcell.00383.2013

Stedman, H. H., Sweeney, H. L., Shrager, J. B., Maguire, H. C., Panettieri, R. A., Petrof, B., . . . Kelly, A. M. (1991). The mdx mouse diaphragm reproduces the degenerative changes of Duchenne muscular dystrophy. *Nature, 352*(6335), 536-539. doi:10.1038/352536a0

Trotter, J. A., & Purslow, P. P. (1992). Functional morphology of the endomysium in series fibered muscles. *J Morphol, 212*(2), 109-122. doi:10.1002/jmor.1052120203

Turgeman, T., Hagai, Y., Huebner, K., Jassal, D. S., Anderson, J. E., Genin, O., . . . Pines, M. (2008). Prevention of muscle fibrosis and improvement in muscle performance in the mdx mouse by halofuginone. *Neuromuscul Disord, 18*(11), 857-868. doi:10.1016/j.nmd.2008.06.386

van Zwieten, R. W., Puttini, S., Lekka, M., Witz, G., Gicquel-Zouida, E., Richard, I., . . . Mermod, N. (2013). Assessing dystrophies and other muscle diseases at the nanometer scale by atomic force microscopy. *Nanomedicine, 9*(4), 393-406. doi:10.2217/nnm.12.215

Veronda, D. R., & Westmann, R. A. (1970). Mechanical characterization of skin-finite deformations. *J Biomech, 3*(1), 111-124.

Virgilio, K. M., Martin, K. S., Peirce, S. M., & Blemker, S. S. (2015). Multiscale models of skeletal muscle reveal the complex effects of muscular dystrophy on tissue mechanics and damage susceptibility. *Interface Focus, 5*(2), 20140080. doi:10.1098/rsfs.2014.0080

Wang, S., & Larin, K. V. (2014). Shear wave imaging optical coherence tomography (SWI-OCT) for ocular tissue biomechanics. *Optics Letters, 39*(1), 41-44.

Wang, S., Larin, K. V., Li, J., Vantipalli, S., Manapuram, R. K., Aglyamov, S., . . . Twa, M. D. (2013). A focused air-pulse system for optical-coherence-tomography-based measurements of tissue elasticity. *Laser Physics Letters, 10*(7), 075605.

Wang, S., Li, J., Manapuram, R. K., Menodiado, F. M., Ingram, D. R., Twa, M. D., . . . Larin, K. V. (2012). Noncontact measurement of elasticity for the detection of soft-tissue tumors using phase-sensitive optical coherence tomography combined with a focused air-puff system. *Optics Letters, 37*(24), 5184-5186. doi:10.1364/OL.37.005184

Wang, S., Lopez, A. L., Morikawa, Y., Tao, G., Li, J., Larina, I. V., . . . Larin, K. V. (2014). Noncontact quantitative biomechanical characterization of cardiac muscle using shear wave imaging optical coherence tomography. *Biomedical Optics Express, 5*(7), 1980-1992. doi:10.1364/BOE.5.001980

Webster, D. R., Wehland, J., Weber, K., & Borisy, G. G. (1990). Detyrosination of alpha tubulin does not stabilize microtubules in vivo. *J Cell Biol, 111*(1), 113-122.

Whitehead, N. P., Kim, M. J., Bible, K. L., Adams, M. E., & Froehner, S. C. (2015a). A new therapeutic effect of simvastatin revealed by functional improvement in muscular dystrophy. *Proc Natl Acad Sci U S A*. doi:10.1073/pnas.1509536112

Whitehead, N. P., Yeung, E. W., Froehner, S. C., & Allen, D. G. (2010). Skeletal muscle NADPH oxidase is increased and triggers stretch-induced damage in the mdx mouse. *PLoS.One., 5*(12), e15354. doi:10.1371/journal.pone.0015354 [doi]

Wilson, C., & Gonzalez-Billault, C. (2015). Regulation of cytoskeletal dynamics by redox signaling and oxidative stress: implications for neuronal development and trafficking. *Front Cell Neurosci, 9*, 381. doi:10.3389/fncel.2015.00381

Wolff, A. V., Niday, A. K., Voelker, K. A., Call, J. A., Evans, N. P., Granata, K. P., & Grange, R. W. (2006). Passive mechanical properties of maturing extensor digitorum longus are not affected by lack of dystrophin. *Muscle & Nerve, 34*(3), 304-312. doi:10.1002/mus.20588

Wood, L. K., Kayupov, E., Gumucio, J. P., Mendias, C. L., Claflin, D. R., & Brooks, S. V. (2014). Intrinsic stiffness of extracellular matrix increases with age in skeletal muscles of mice. *Journal of Applied Physiology, 117*(4), 363-369. doi:10.1152/japplphysiol.00256.2014

Table 1. Tubulin and stiffness correlations

Adj R^2	Fibrosis	α-tubulin	β-tubulin	DT-tubulin	DT-/α-tubulin	MLR (fibrosis/glu)	MLR (fibrosis/ratio)
Transverse	0.69 *	0.46 *	0.51 *	0.51 *	0.10	0.69	0.67
Longitudinal	0.44 *	0.20 *	0.40 *	0.41 *	0.19 *	0.44	0.49

Most variables significantly correlated with both transverse and longitudinal stiffness. MLR revealed fibrosis accounted for the majority of the variance observed in either stiffness measure. $p \leq 0.05$ *Significant correlation in at least $n_{animals}=6$.

Table 2. Force and stiffness correlations

Adj R^2	Fibrosis	MLR (fibrosis/trans)	MLR (fibrosis/long)	MLR (fibrosis/long/trans)
Force	0.57	0.52	0.52	0.49

MLR revealed fibrosis accounted for a majority of the variance observed in diaphragm muscle function. $p \leq 0.05$ *Significant difference between groups in at least $n_{animals}=6$.

Table 3. Respiratory function

	WT	*mdx*	$p47^{(-/-)}$/*mdx*
f (breath/min)	408.2 ± 14.5 *	279.8 ± 18.3	377.3 ± 17.0 *
T_v (ml)	0.25 ± .009	0.24 ± .008	0.26 ± .012
M_v (ml)	100.3 ± 5.6 *	65.9 ± 17.6	99.2 ± 8.6 *
PIF (ml/s)	7.6 ± 0.30 *	5.9 ± 0.56	8.0 ± 0.51 *
PEF (ml/s)	4.2 ± 0.25	3.2 ± 0.24	4.4 ± 0.39 *
T_i (s)	0.057 ± .002 *	0.080 ± .007	0.057 ± .002 *
T_e (s)	0.129 ± .009 *	0.190 ± .012	0.138 ± .008 *

Dystrophic mice lacking Nox 2 ROS production maintained respiratory function similar to WT levels. $p \leq 0.05$ *Significant difference vs. *mdx* in at least $n_{animals}=9$.

Figure 1. Eliminating Nox 2 ROS production prevents alterations in tubulin content and the microtubule network. A. Representative western blot images of α-, β-, and DT-tubulin content in all three genotypes. **B-D.** Eliminating Nox2 ROS production decreases absolute α-, β- and DT-tubulin content in dystrophic diaphragm muscle. **E.** The relative amount of DT-/α-tubulin is not different between groups. **F.** Representative images of diaphragm myofibers stained with α-tubulin. **G-I.** The lack of Nox 2 ROS prevents microtubule disorganization and the increase in microtubule density seen in *mdx* muscle. $p \leq 0.05$ *Significant difference between groups in at least (A-E) $n_{animals} = 6$ and (F-I) $n_{animals} = 3$ and $n_{fibers} = 15$.

Figure 2. Genetic deletion of Nox2 ROS production reduced fibrosis.
A. Representative trichrome images of fibrosis in all three genotypes. Eliminating Nox2 ROS production in dystrophic muscle reduced fibrosis compared with *mdx* mice. **B.** Hydroxyproline levels were elevated in dystrophic muscle and eliminating Nox2 ROS reduced hydroxyproline content compared with *mdx* mice. **C.** Representative western blot images for fibronectin and collagen I content in all three genotypes. Fibronectin and collagen I content were elevated in *mdx* diaphragm and eliminating Nox2 ROS reduced both toward WT levels. $p \leq 0.05$ * Significant difference between groups in at least $n_{animals}=6$ for trichrome and hydroxyproline and $n_{animals}=3$ for fibronectin and collagen I.

Figure 3. The lack of Nox2 ROS reduces muscle stiffness and stretch induced ROS.
A. Image of the passive stretch experimental set-up. **B.** Average passive diaphragm force recorded during stretch for each genotype. **C.** Eliminating Nox2 ROS production reduced diaphragm tissue stiffness. **D.** Stretch induced ROS in *mdx* muscle was elevated above WT levels and eliminated in $p47^{-/-}$/*mdx* diaphragm. **E.** Image of the OCE experimental set-up. **F.** Representative OCT image of the diaphragm taken prior to OCE experiments. **G.** Transverse diaphragm muscle stiffness increased in *mdx* compared with WT mice; eliminating Nox2 ROS resulted in a decrease toward WT ($p=0.09$). **H.** Genetic inhibition of Nox2 ROS reduced longitudinal diaphragm stiffness to WT values. **I.** Muscle function was not altered following OCE measurements. $p \leq 0.05$ *Significant difference between groups in at least $n_{animals}=6$ per group.

Figure 4. Eliminating Nox2 ROS protects against muscle and respiratory dysfunction.
A. WT was significantly different from *mdx* and $p47^{-/-}$/*mdx* animals at all stimulation frequencies. The $p47^{-/-}$/*mdx* animals were different from *mdx* at 60-100 Hz and trended towards significance at 40 Hz ($p=0.098$). **B.** Fibrosis significantly correlated with muscle force. $p \leq 0.05$ *Significant difference between groups in at least $n_{animals}=6$.

Figure 5. Taxol induced MT polymerization has no effect on tissue stiffness but induced ROS production. A. Representative images of MT network in control (DMSO) and Taxol treated diaphragm (20 μM for 2 hr). **B-D.** Taxol induced MT disorganization and increased microtubule density compared with control. **E.** Average passive diaphragm force recorded during stretch was not affected by Taxol. **F.** Polymerizing the MT network had no effect on diaphragm tissue stiffness. **G.** MT network polymerization enhanced stretch induced ROS in Taxol treated diaphragm. $p \leq 0.05$ *Significant difference between groups in at least (A-D) $n_{animals} = 3$ and $n_{fibers} = 15$ and (E-G) $n_{animals} = 5$.

Supplemental Figure Legends

Figure 3- video 1

Longitudinal. Following the application of the air puff (<1 ms in duration), the displacement of the diaphragm tissue was monitored as the wave propagated down longitudinal axis while imaged at 62.5 kHz with OCE. Visualization is 5000 times slower than the actual speed.

Figure 4-figure supplement 1 Eliminating Nox2 ROS protects against phenotypic alterations in dystrophic diaphragm muscle.

A-B. Eliminating Nox2 ROS increased median cross sectional area compared with *mdx* diaphragm. **C.** In dystrophic diaphragm lacking Nox2 ROS production the number of centralized nuclei were reduced compared with *mdx* diaphragm tissue. **D.** Representative hematoxylin and eosin stained images of diaphragm cross-section showing central nuclei (arrow head) and smaller fibers (arrow). **E.** Fiber type distribution was maintained by eliminating Nox2 ROS production in dystrophic diaphragm muscle. **F.** Representative immunofluorescently labeled diaphragm cross-sectional images showing fiber type distribution. Type I (red), IIA (green), IIB/IIX (white x, unstained and viewed from bright field overlay). $p \leq 0.05$ *Significant difference between groups in at least $n_{animals}=3$.

Figure 4-figure supplement 2 Linear correlation of stiffness measured by OCE and the peak force

There was a significant correlation between peak force and transverse as well as peak force and longitudinal diaphragm stiffness.

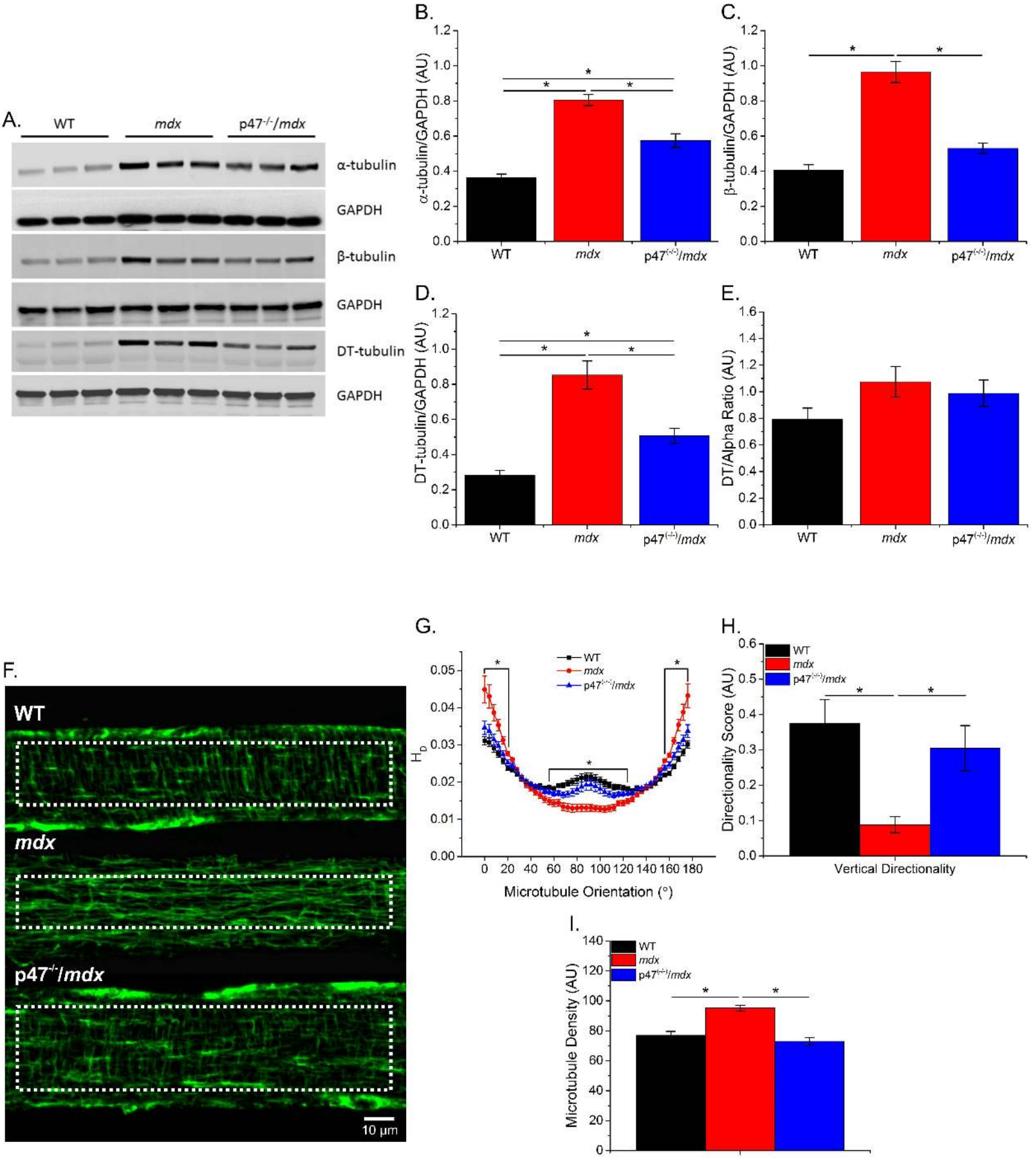
A.
WT
mdx
p47-/-/mdx
α-tubulin
GAPDH
β-tubulin
GAPDH
DT-tubulin
GAPDH
B.
α-tubulin/GAPDH (AU)
WT
mdx
p47(-/-)/mdx
C.
β-tubulin/GAPDH (AU)
D.
DT-tubulin/GAPDH (AU)
E.
DT/Alpha Ratio (AU)
F.
WT
mdx
p47-/-/mdx
10 μm
G.
WT
mdx
p47(-/-)/mdx
HD
Microtubule Orientation (°)
H.
Directionality Score (AU)
Vertical Directionality
I.
Microtubule Density (AU)

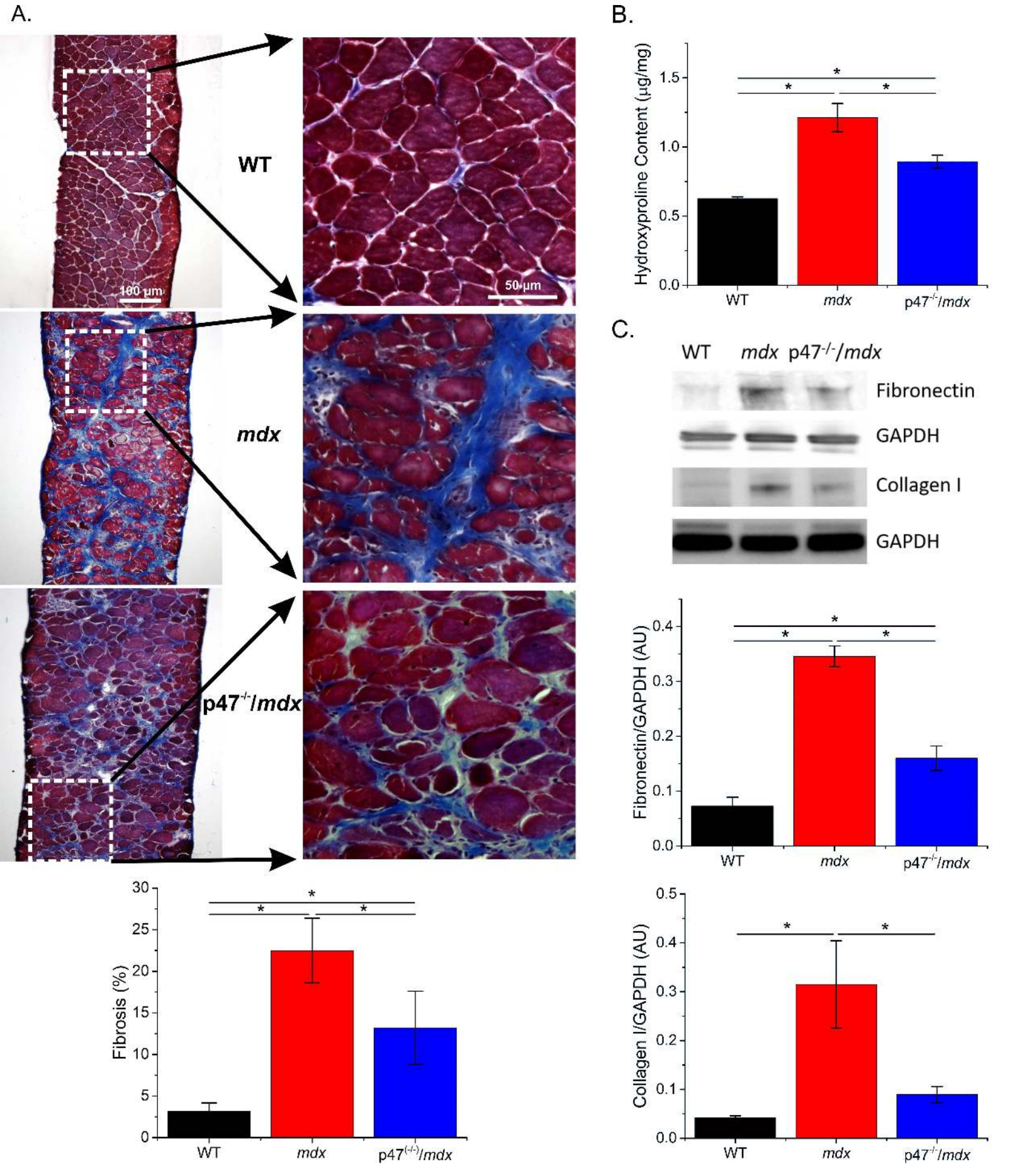
A.
WT
mdx
p47-/-/mdx
100 µm
50 µm
B.
Hydroxyproline Content (µg/mg)
1.5
1.0
0.5
0.0
WT
mdx
p47-/-/mdx
C.
WT
mdx
p47-/-/mdx
Fibronectin
GAPDH
Collagen I
GAPDH
Fibronectin/GAPDH (AU)
0.4
0.3
0.2
0.1
0.0
WT
mdx
p47-/-/mdx
Fibrosis (%)
30
25
20
15
10
5
0
WT
mdx
p47(-/-)/mdx
Collagen I/GAPDH (AU)
0.5
0.4
0.3
0.2
0.1
0.0
WT
mdx
p47-/-/mdx

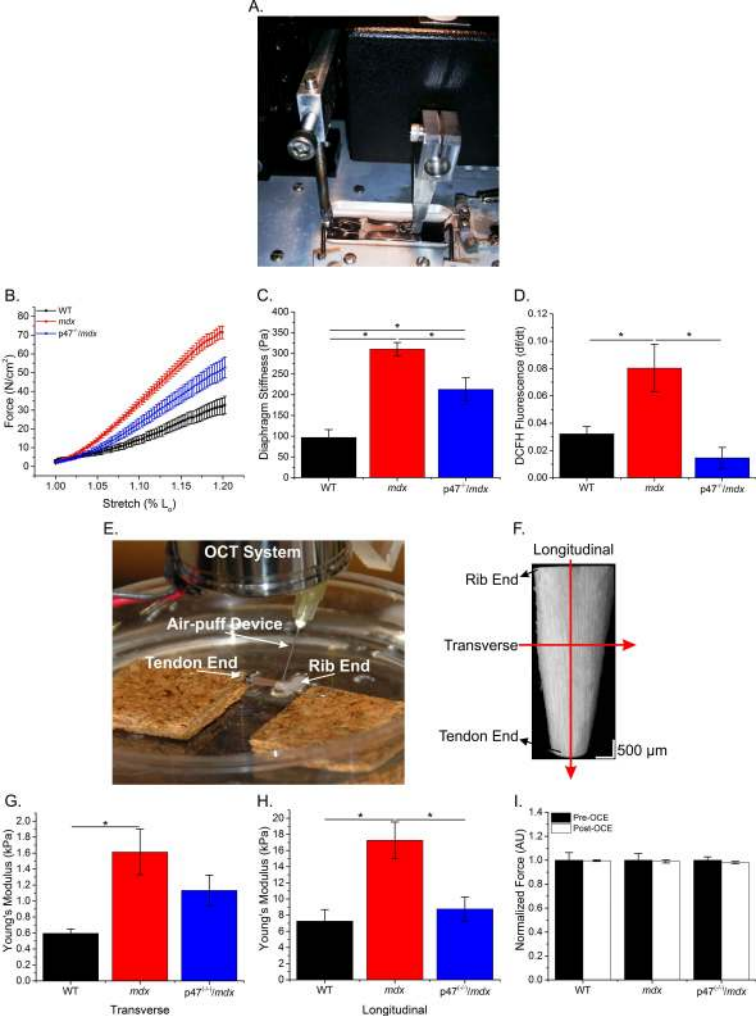
A.
B.
WT
mdx
p47-/-/mdx
Force (N/cm2)
Stretch (% L0)
C.
Diaphragm Stiffness (Pa)
WT
mdx
p47-/-/mdx
D.
DCFH Fluorescence (dF/dt)
WT
mdx
p47-/-/mdx
E.
OCT System
Air-puff Device
Tendon End
Rib End
F.
Longitudinal
Rib End
Transverse
Tendon End
500 µm
G.
Young's Modulus (kPa)
WT
mdx
p47-/-/mdx
Transverse
H.
Young's Modulus (kPa)
WT
mdx
p47-/-/mdx
Longitudinal
I.
Pre-OCE
Post-OCE
Normalized Force (AU)
WT
mdx
p47-/-/mdx

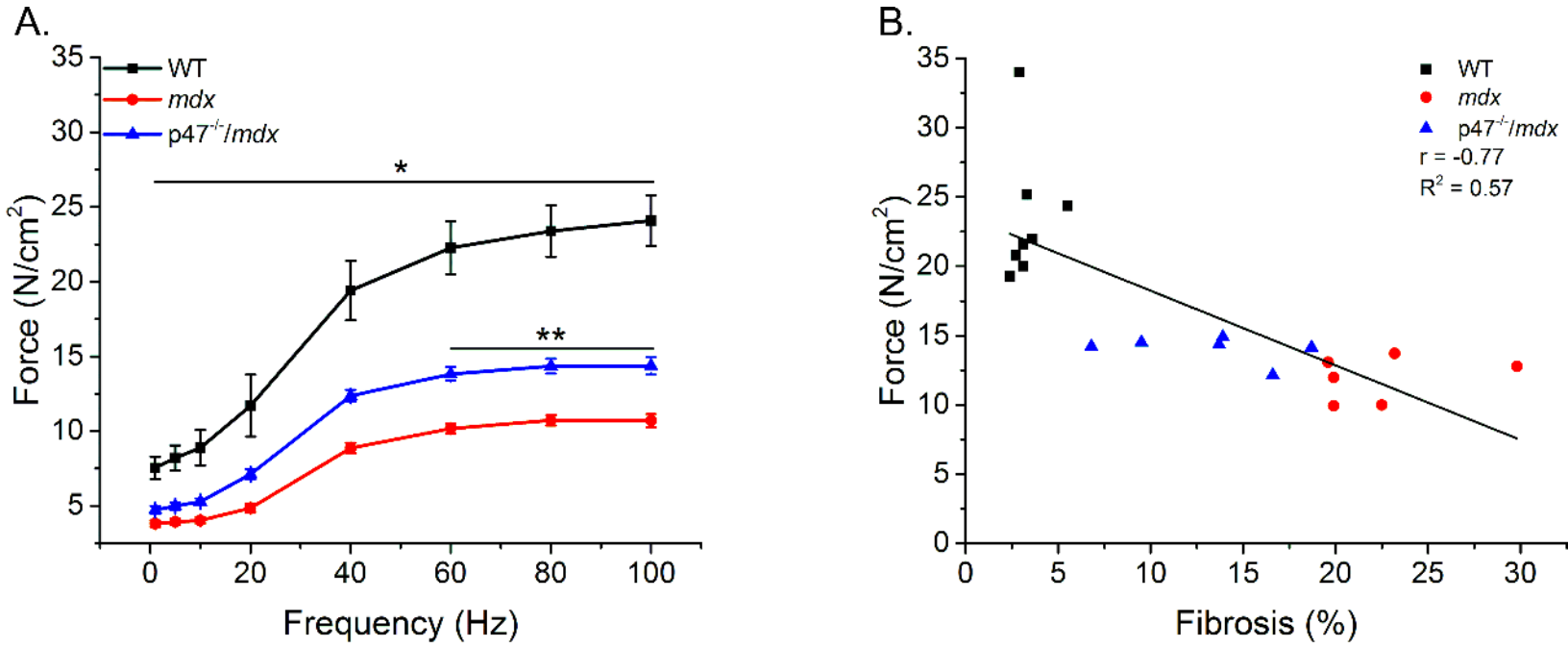
A.
WT
mdx
p47-/-/mdx
*
**
Force (N/cm2)
Frequency (Hz)
0
20
40
60
80
100
5
10
15
20
25
30
35
B.
WT
mdx
p47-/-/mdx
r = -0.77
R2 = 0.57
Force (N/cm2)
Fibrosis (%)
0
5
10
15
20
25
30

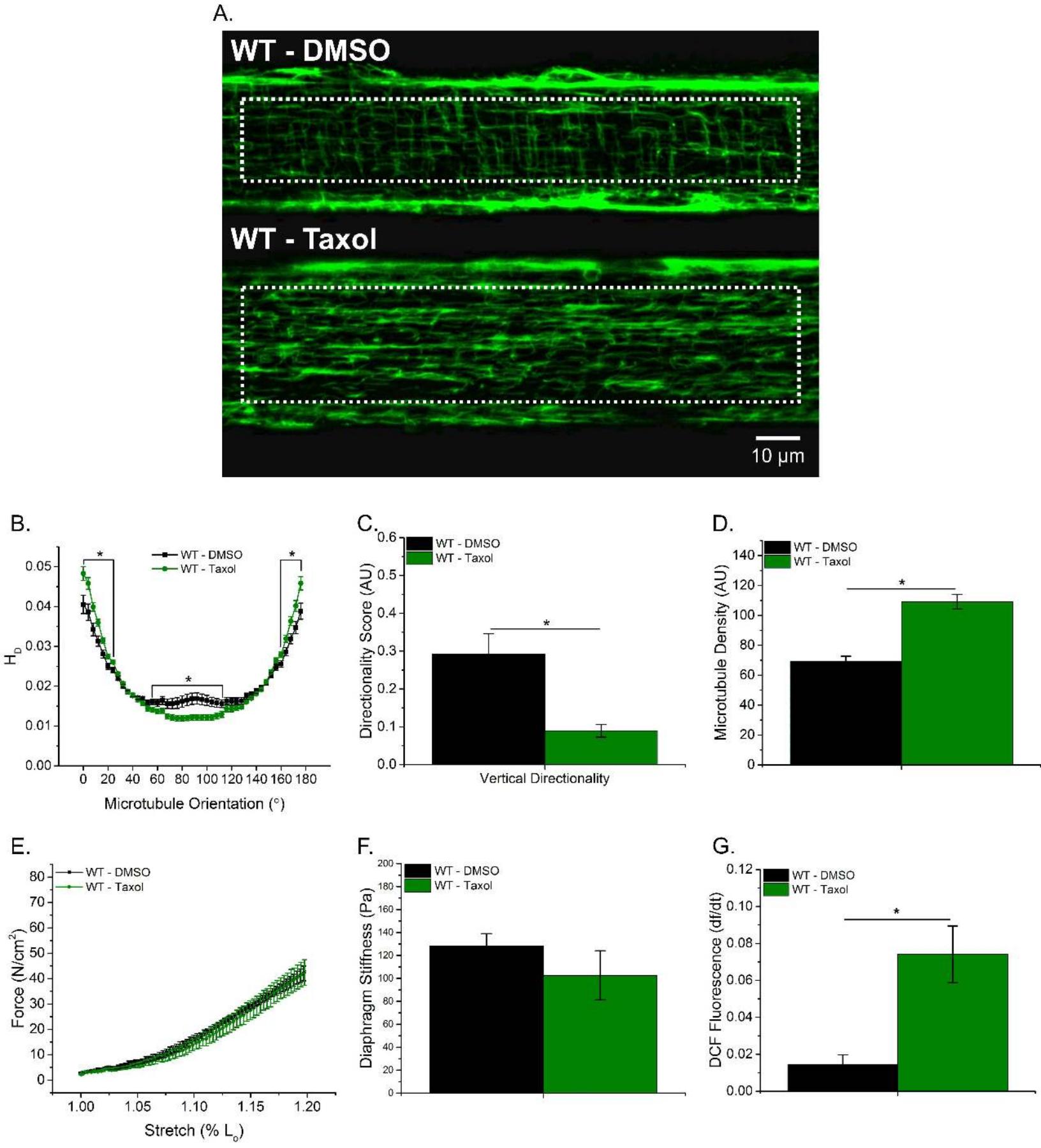
A.
WT - DMSO
WT - Taxol
10 µm
B.
WT - DMSO
WT - Taxol
H_D
Microtubule Orientation (°)
C.
WT - DMSO
WT - Taxol
Directionality Score (AU)
Vertical Directionality
D.
WT - DMSO
WT - Taxol
Microtubule Density (AU)
E.
WT - DMSO
WT - Taxol
Force (N/cm^2)
Stretch (% L_o)
F.
WT - DMSO
WT - Taxol
Diaphragm Stiffness (Pa)
G.
WT - DMSO
WT - Taxol
DCF Fluorescence (df/dt)

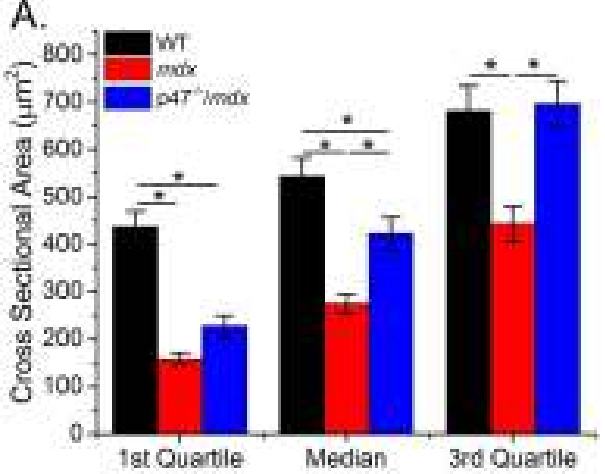
A.
WT
mdx
p47-/-/mdx
Cross Sectional Area (μm2)
1st Quartile
Median
3rd Quartile

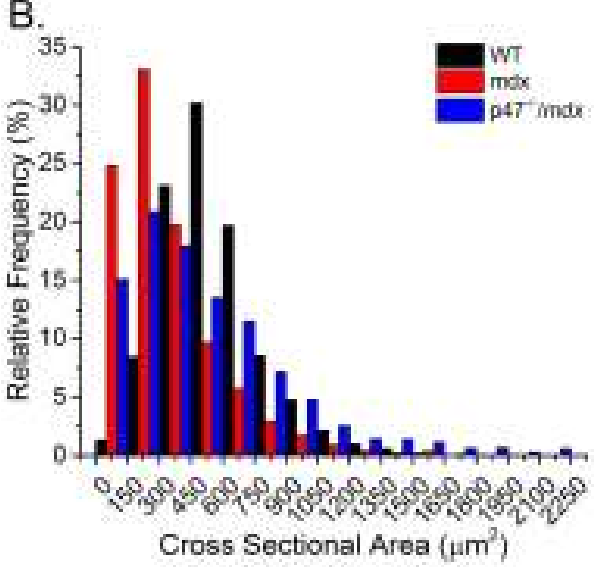
B.
WT
mdx
p47-/-/mdx
Relative Frequency (%)
Cross Sectional Area (μm2)

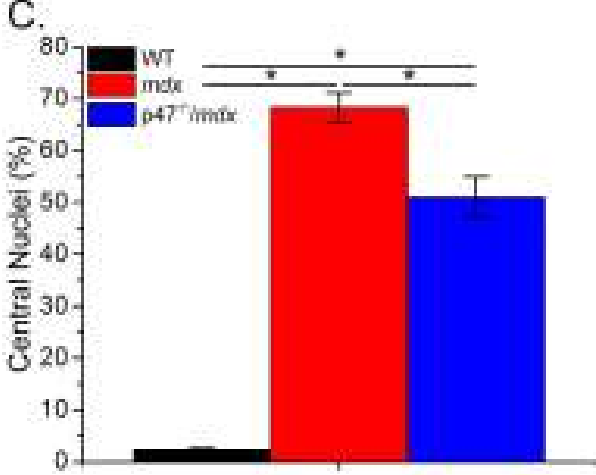
C.
WT
mdx
p47-/-/mdx
Central Nuclei (%)

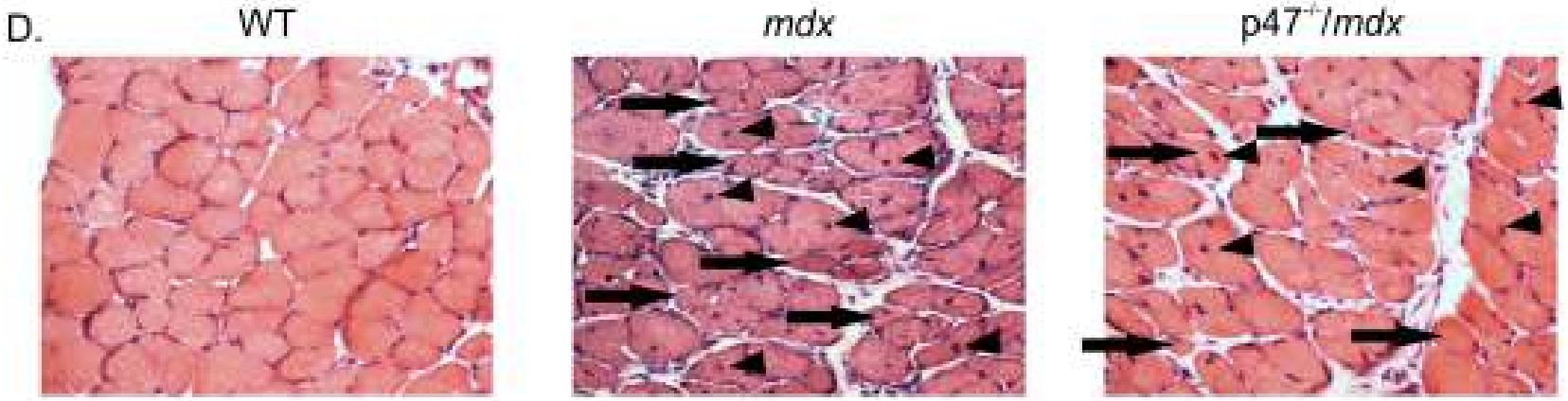
D.
WT
mdx
p47-/-/mdx

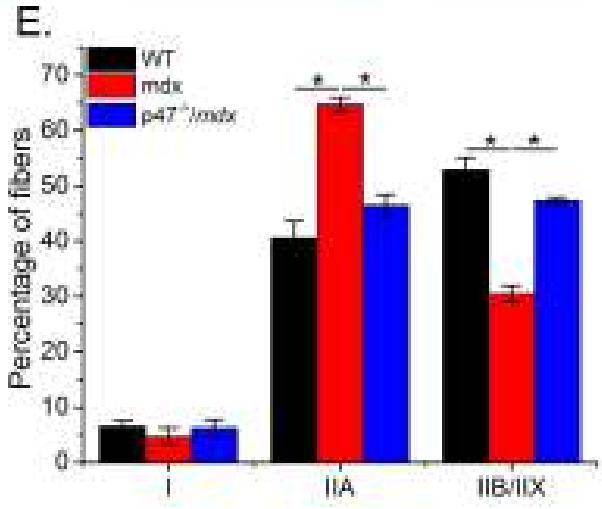
E.
WT
mdx
p47-/-/mdx
Percentage of fibers
I
IIA
IIB/IIX

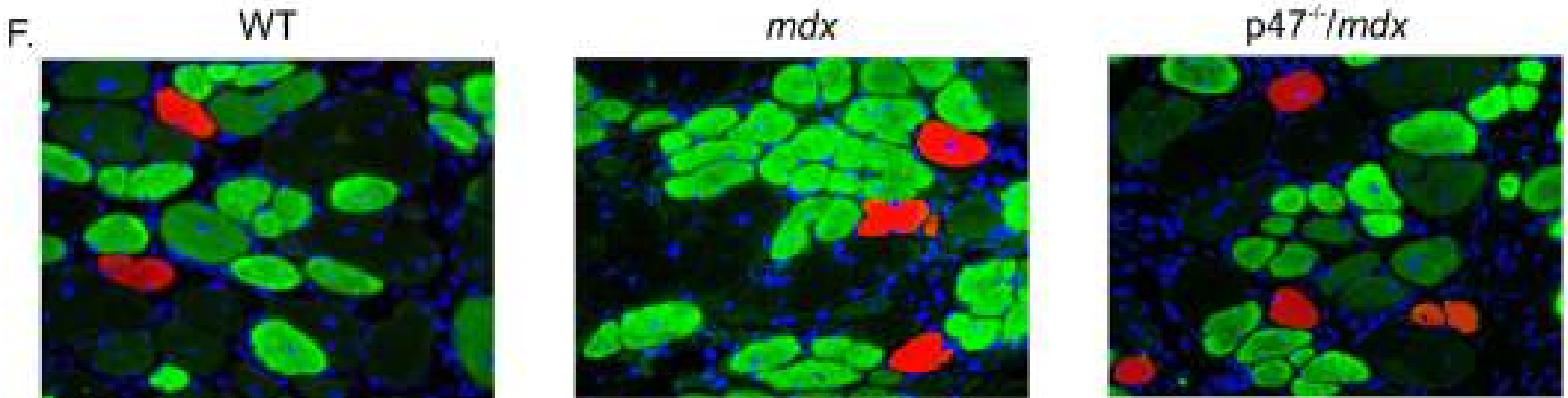
F.
WT
mdx
p47-/-/mdx

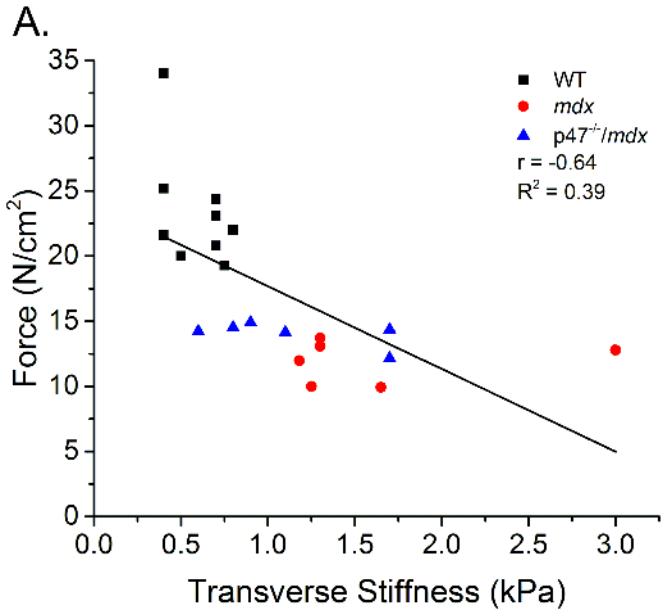
A.
WT
mdx
p47-/-/mdx
r = -0.64
R2 = 0.39
Force (N/cm2)
Transverse Stiffness (kPa)
0
5
10
15
20
25
30
35
0.0
0.5
1.0
1.5
2.0
2.5
3.0

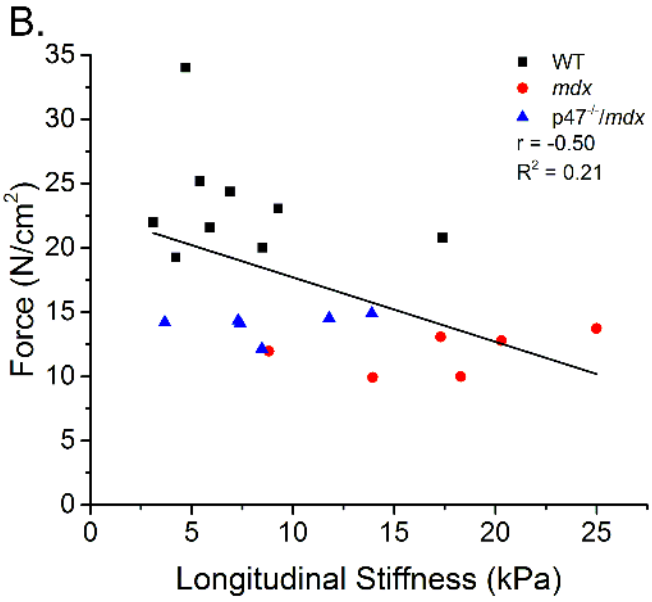
B.
WT
mdx
p47-/-/mdx
r = -0.50
R2 = 0.21
Force (N/cm2)
Longitudinal Stiffness (kPa)
0
5
10
15
20
25
30
35